REVIEW

Upconversion nanophosphors for solar cell applications

Parthiban Ramasamy, Palanisamy Manivasakan and Jinkwon Kim*

Currently, one of the major factors limiting the efficiency of solar cells is the spectral mismatch between the energy distribution of photons in the incident solar spectrum and the bandgap of a semiconductor material. To reduce spectral mismatch losses, wavelength conversion of sunlight is regarded as an effective route. Both upconversion and downconversion materials are currently being explored as spectral converters for solar cells. In an upconversion process, photons with energy lower than the band gap of the solar cell are converted to higher energy photons that can be absorbed by the semiconductor. This review focuses on the various synthetic approaches to upconversion nanocrystals and methods to improve upconversion luminescence, as well as it gives an overview of the recent developments in the photovoltaic applications of upconversion nanomaterials.

1. Introduction

Global energy consumption is increasing and is expected to double by the end of 2050. Most of our energy supply comes from fossil fuels; however, their finite nature and the environmental concerns associated with fossil fuels have triggered the search for alternative renewable energy sources.[1,2] There exist many potential renewable energy technologies such as biomass, geothermal, hydrogen fuel cells, hydropower, ocean, wind and solar energy technology. Sunlight is a freely available abundant source of solar energy, and it irradiates the Earth's surface with 120 000 TW of solar power. It has been reported that the Earth's surface receives nearly 10 000 times more sunlight than what we consume.[3] Harnessing solar energy through photovoltaic (PV) technology has the potential to meet our energy demands in a cleaner way.

A solar cell is a photovoltaic device that converts light photons directly into electricity. Solar cells are anticipated to create a sustainable future with considerable energy economy through the development of solar energy technology. Environmentally benign solar cells are essentially required to power electricity-demanding areas such as transportation, stationary and portable applications. In general, solar cells are divided into different generations, namely, first, second and third generations.[4] Both single-crystalline and polycrystalline silicon wafers have been primarily used for the fabrication of first-generation solar cells. Silicon solar cell technology is a well-developed and the most utilized system, achieving a

Department of Chemistry and GETRC, Kongju National University, 182, Shinkwondong, Kongju, 314-701, Chungnam-do, Republic of Korea. E-mail: jkim@kongju.ac.kr; Fax: +82-41-850-8613; Tel: +82-41-850-8496

Parthiban Ramasamy completed his MSc degree (2010) in Chemistry from Madurai Kamaraj University, India. He is currently pursuing his PhD degree under the supervision of Prof. Jinkwon Kim in the Department of Chemistry at Kongju National University, South Korea. His research interest focuses on the synthesis of inorganic nanomaterials for energy conversion and storage applications.

Palanisamy Manivasakan earned his Master's degree in Chemistry from The Gandhigram Rural Institute, India in 2006. He received his PhD degree in Chemistry from Anna University, Chennai under the supervision of Prof. Venkatachalam Rajendran in 2013. He is currently working with Prof. Jinkwon Kim as a postdoctoral fellow in the Department of Chemistry at Kongju National University, South Korea. His research interest focuses on the synthesis of nanomaterials for energy applications.

maximum efficiency of 25%. Unfortunately, the cells are expensive to produce and the market cost is dominated by the high purification cost of silicon substrates.[5] The second-generation solar cells have been developed to reduce the usage of high-cost materials. The second generation is mainly based on thin-film solar cells that are produced cheaply such that the cost per watt is lower than with the first-generation cells. Thin-film solar cells such as CIGS (Cu, In, Ga, Se), CdTe, and amorphous silicon are the most popular in the second generation and have maximum cell efficiencies of 20.8%, 20.4%, and 13.4%, respectively. Nevertheless, the efficiency of thin-film solar cells is still lower than with first-generation silicon cells and several second-generation cells rely on scarce and toxic materials.[6] Both first- and second-generation solar cells suffered from the Shockley–Queisser limit, which states that a single-junction solar cell with band gap equal to 1.1 eV can only have a maximum efficiency of 31%.[7] Third-generation solar cells have the potential to overcome the Shockley–Queisser limit and are considered as potential alternatives to expensive first and toxic second-generation solar cells. They are inexpensive, have a simple fabrication process and, importantly, can be printed on large areas and flexible substrates. It comprises of solar cell technologies such as dye-sensitized solar cells (DSSCs),[8,9] colloidal quantum dot solar cells,[10] organic photovoltaics[11,12] and solution-processed bulk inorganic photovoltaics.[13] Most of the third-generation technologies are not yet commercialised, but there is a lot of research going on in this area. In the third and present generation, work is under way to make inexpensive solar cells with high efficiency.

For any single-junction solar cell, the band gap (E_g) of the semiconductor, which is used to construct the solar cell, determines the maximum conversion efficiency.[14] Fig. 1 shows a schematic diagram of the loss mechanisms that affect the efficiency of single-junction solar cells. There are two major loss mechanisms that need to be addressed to enhance solar cell efficiencies: lattice thermalisation and transparency to sub-band gap photons.

When a semiconductor absorbs a photon of higher energy than the band gap, an electron–hole (e–h) pair with higher
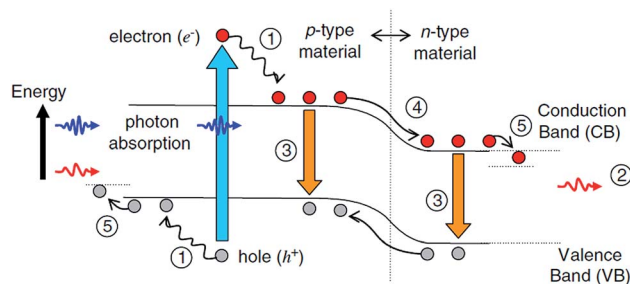

Fig. 1 Loss processes in a single-junction solar cell: (1) lattice thermalisation loss; (2) transparency; (3) recombination loss; (4) junction loss and (5) contact voltage loss. Reprinted with permission from ref. 14. Copyright 2006, Elsevier.

energy is created and the excess energy is dissipated as heat. This is known as thermalisation loss. On the other hand, photons with energy lower than the band gap are not absorbed by the semiconductor and are transmitted. Thermalisation losses are high in solar cells with a smaller band gap, whereas transmission losses contribute more to the losses for wider band gap solar cells. A further loss mechanism is the recombination of e–h pairs close to or at the surface, and this loss process can be minimized through maintaining high minority carrier lifetimes in the semiconductor material. About 70% of the energy loss is related to thermalisation and transmission energy losses and is termed spectral mismatch. This mainly results from the spectral mismatch between the incident solar spectrum and the band gap of the semiconductors.

In order to tackle spectral mismatch, solar cells with a series-connect stack of two to five junctions (multi-junction solar cells) made from semiconducting materials with a decreasing band gap are proposed. A multi-junction solar cell that covers a range of the solar spectrum with different wavelengths has greatly increased the efficiency of solar cells and almost reached twice the efficiency of single-junction cells. Compared to all other single-junction solar cells, multi-junction solar cells have the highest theoretical limit of efficiency and produce a maximum recorded efficiency of 43.5%.[15] However, multi-junction solar cells are much more complex than the single-junction versions. This increased complexity greatly increases the production cost and it is relatively expensive for global use. Thus, single-junction solar cells are most commonly used nowadays. Many strategies are under investigation for achieving efficient light absorption, charge separation, transport and collection in single-junction solar cells.[16–18] Even though many light-harvesting methods are available for trapping a wide range of the solar spectrum, there is still a need for enhanced photon absorption technology for the development of highly efficient solar cells.

Wavelength conversions of light photons are a promising route to reduce spectral mismatch losses that are considered to be the major part of the efficiency losses in single-junction solar cells. In recent years, wavelength-dependent spectral converters have been explored for enhanced energy conversion in single-junction solar cells. There are three luminescence processes, namely, quantum cutting, downshifting and upconversion,

Jinkwon Kim was born in Seoul, Korea. He earned his BS degree (1986) in Chemistry from Seoul National University. He received his PhD (1992) in Chemistry from Korea Advanced Institute of Science and Technology (KAIST) under the direction of Prof. Youngkyu Do. He then became a postdoctoral fellow in the group of Prof. Joel S. Miller at the University of Utah. He joined the faculty of Kongju National University in 1993. His current research interests include the synthesis and self-assembly of nanoscaled materials for energy conversion and storage applications.

which have the potential to increase solar cell efficiencies. Quantum cutting through downconversion is able to cut one high-energy photon into multiple low-energy photons with a conversion efficiency higher than 100%.[19] Quantum cutting reclaims some of the excess energy of high-energy photons through the downconversion process and downconverted photons can be absorbed by solar cells, which minimizes the energy loss and increases the conversion efficiency. A subcategory of downconversion is the downshifting process that occurs at sub-unity quantum efficiencies and involves transformation of one absorbed high-energy photon into one lower-energy photon. Both downshifting and quantum cutting are interrelated, but in the case of downshifting, the efficiency cannot exceed 100%. Downshifting can effectively convert short-wavelength ultraviolet light to longer-wavelength visible light, for which the solar cells have maximum response.

Upconversion is a process where low-energy photons (infrared and near-infrared) are converted into high-energy visible photons. This process could enable the conversion of incident light with energies lower than the semiconductor band gap and can significantly reduce transmission energy losses. In 2002, Trupke and Green et al.[20] proposed that the upconversion of sub-band gap light can result in significant improvements in the conversion efficiency of solar cells. They investigated a system of bifacial silicon solar cells with upconversion layers placed on the rear side. The upper limit of the energy conversion efficiency of the system was found to be 63.2% for concentrated sunlight and 47.6% for non-concentrated sunlight. This model boosted research on upconversion solar cells.

In this review, we focus on the light absorption enhancement of single-junction solar cells through a selective upconversion process. First, we describe the basic concepts of upconversion luminescence. Second, we describe the recent developments in the synthesis of various upconversion nanomaterials by the thermal decomposition method, hydro/solvothermal method, co-precipitation method, microwave-assisted method (Table 1) and ionic liquid-based synthesis. The third section describes some important strategies to improve upconversion photoluminescence. Finally, we highlight the recent research progress in the application of upconverter materials in various solar cells such as crystalline silicon, amorphous silicon, DSSC and organic solar cells. The summary of the present review will give a positive insight on the topic of upconversion nanomaterial application in solar cells.

2. Upconversion luminescence

2.1. Upconversion mechanism

Upconversion (UC) is a unique type of photoluminescence, in which lower-energy excitation (near-infrared light) is converted into higher-energy emission (visible light) via multi-photon absorption processes. This phenomenon was first discovered by Auzel in the 1960s.[21] Generally, the UC process is observed in lanthanide or transition metal ions doped in an inorganic host and to some extent in organic chromophores with an extended conjugated π-system.[21–23] UC processes can be mainly divided

into three broad classes: excited-state absorption (ESA), energy transfer upconversion (ETU), and photon avalanche (PA). All these processes involve the population of a highly excited state by sequential absorption of two or more photons by metastable, long-lived energy states.

In excited-state absorption, a single emitting ion with ladder-like energy levels sequentially absorbs two (or more) photons using a real intermediary energy level and is promoted to a higher excited state. The general energy diagram of the ESA process is shown in Fig. 2 for a simple three-level system. The energy difference between the levels G and E1 is similar to that for levels E1 and E2, which facilitates the ESA mechanism. When the excitation energy is resonant with the transition from ground level G to excited metastable level E1, a process known as ground-state absorption (GSA) takes place and populates the E1 level. The ion in the E1 level has a high possibility of being promoted to the E2 level by another pump photon due to the long lifetime of the E1 state before its decay to the ground state. The upconversion emission occurs from the E2 level.

Energy transfer upconversion is quite different from ESA, as ESA takes place within a single lanthanide ion, while ETU involves two neighbouring ions. In an ETU process, each of two neighbouring ions can absorb a pump photon of the same energy by GSA, thereby populating the metastable level E1. A non-radiative energy transfer promotes one of the ions to the upper emitting state E2, while the other ion relaxes back to the ground state G. The upconversion efficiency of an ETU process is highly sensitive to the average distance between the two neighbouring ions, which is determined by the concentrations of dopants.

Chivian and co-workers first discovered the phenomenon of photon avalanche in Pr^{3+} infrared quantum counters.[24] PA is a process that produces UC above a certain threshold of excitation power. It is a looping process that involves ESA processes for excitation light and an efficient cross-relaxation (CR) that produces feedback. First, the E1 level of ion 2 is populated by weak non-resonant GSA, followed by resonant ESA to populate the level E2. An efficient CR energy transfer occurs between the excited ion 2 and a neighbouring ground state ion 1, resulting in both ions occupying the intermediate level E1. Finally, ion 1 transfers its energy to ion 2 to populate its E1 level and completes the loop. The net result produces two ion 2s at E1 level. One of them absorbs the excitation radiation and is excited to the E2 state, in which it interacts with the ground state of ion 1 by CR to form three ion 2s at E1 level. By repeating the whole steps again and again, the E2 level of ion 2 is increased dramatically and produces strong UC emission.

2.2. Upconversion in lanthanide ions

A typical inorganic UC phosphor contains a crystalline host material and a dopant (emitter) added in low concentration. The dopant acts as luminescent centers while the host provides a crystalline matrix to bring these centers into optimal positions. The presence of multiple metastable levels in lanthanide ions makes them a preferred dopant for UC inorganic phosphors. The lanthanides, which are characterized by the

Table 1 Typical upconversion host materials and their synthetic methods

Hydro(solvo)thermal method

Host	Surfactant	Shape	Ref.
$NaYF_4$	OA	Sphere, nanoplate, nanorod, nanotube, nanodisk	97–10, 102 and 122
	Cit^{3-}	Microplate	109–111
	EDTA	Sphere	113
	PVP	Sphere	115
	PEI	Sphere	117–120
	PAA	Nanorod	121
$NaGdF_4$	OA	Sphere, polyhedron	104 and 122
$NaREF_4$ (RE = Pr, Nd, Sm, Eu, Dy, Ho, Er, Tm, Tb)	OA	Polyhedron, nanotube, nanodisk, nanorod	122
$KGdF_4$	PEI, 6-aminocaproic acid (6AA)	Sphere	123
$BaYF_5$	EDTA	Sphere	114 and 124
	PEI	Sphere	125
BaY_2F_8	OA	Nanobelt	106
Ba_2GdF_7	EG	Pseudo-octahedron	126
Ca_xYF_{3+2x}	CTAB	Microcubic and rhombic	127
CaF_2	OA	Sphere	101
SrF_2	OA	Sphere	103
MnF_2	OA	Nanoclusters and nanolanterns	108
ErF_3	Cit^{3-}, EDTA, PVP, CTAB	Flower-like, microcrystal	128
$PbTiO_3$	Polyvinyl alcohol	Nanofiber	129
GdF_3	PVP	Sphere	130
$GdVO_4$	PVP	Sphere	131
Gd_2O_3	—	Sphere	132
La_2O_3	—	Triagonal or truncated triagonal prism/plate, hexagonal prism	133
Gd_2O_2S	PVP	Submicrosphere	134

Precipitation method

$NaYF_4$	EDTA	Sphere	136
REF_3 (RE = Eu, Er, Nd, and Ho)	Ammonium di-*n*-octadecyl-dithiophosphate	Elongated particle	135
$NaGdF_4$	Na_2EDTA, PVP, SDS, Na_2tar	Rod-shaped aggregate	137
LaF_3	Ammonium di-*n*-octadecyl-dithiophosphate	Sphere	138
Lu_2O_3	Urea	Nano-aggregate, sub-micrometer wire, and nanosphere	139
Y_2O_3	CTAB	Sphere	140

Microwave synthesis

$NaYF_4$	OA	Hexagonal and cubic	142
	—	Sphere, bipyramidal microdisk	143 and 144
$NaGdF_4$	PEI	Quadral cubic, popcorn-like hexagonal	145
$BaYF_5$	PEI	Sphere	146

progressive filling of the 4f orbitals, are a family of 15 chemically similar elements, commencing with lanthanum (La) and ending with lutetium (Lu). Lanthanide ions typically exist in their most stable oxidation state as trivalent ions (Ln^{3+}) and have a $4f^n5s^25p^6$ electron configuration ($0 < n < 14$). Their characteristic optical and magnetic properties arise as a result of the partially filled 4f inner shell. There are 14 over n possible configurations available for lanthanide ions with n number of electrons. This results in a fairly large number of energy level structures.[25] Most of the Ln^{3+} ions show sharp f–f transition bands due to the fact that the 4f electrons of Ln^{3+} ions are shielded by the completely filled $5s^2$ and $5p^6$ sub-shells. The transitions between different $4f^n$ states are Laporte-forbidden, which results in low transition probabilities and substantially long-lived (up to 0.1 s) excited states.[21] Since the excited states of lanthanide ions have longer lifetimes, an excited lanthanide ion may sequentially absorb a second photon of suitable energy at comparatively low excitation densities and reach an ever-higher excited state. When the energy gaps between three or more subsequent energy levels in lanthanide ions are very similar, then they can be excited to a higher excited state using a monochromatic light source, since each absorption step requires the same photon energy. In this sense, Er^{3+}, Tm^{3+}, and Ho^{3+} ions, featuring ladder-like energy levels, were generally
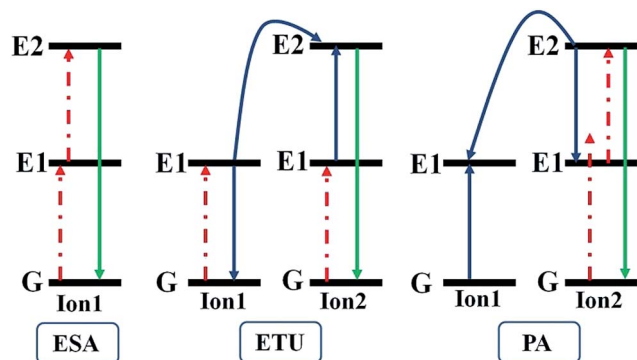
Fig. 2 Principal upconversion processes in lanthanide (Ln^{3+})-doped upconversion nanomaterials.

chosen as emitters to give rise to efficient UC emission.[26] For example, in the Er^{3+} ion the energy difference between the $^4I_{11/2}$ and $^4I_{15/2}$ states (~10350 cm^{-1}) is similar to that between the $^4F_{7/2}$ and $^4I_{11/2}$ states (~10 370 cm^{-1}). In addition, the energy difference between the $^4F_{9/2}$ and $^4I_{13/2}$ states is in the same region; hence, the Er^{3+} ion can be excited to a higher energy level by at least three possible transitions by absorbing IR photons of the same energy, which gives visible upconverted green and red emissions (Fig. 3).

In a singly doped UC phosphor, there are two limiting factors that affect the UC emission intensity: the distance between two

neighbouring emitting ions and the absorption cross-section of the ions. The absorption can be increased by increasing the emitter's concentration in phosphors, but at higher dopant concentrations cross-relaxation may be a severe problem that quenches the excitation energy. In most UC materials, the Er^{3+} and Tm^{3+} concentration does not exceed 3% and 0.5%, respectively. At this low concentration, Er^{3+} and Tm^{3+} ions cannot absorb the excitation light effectively, which results in low UC efficiency.

In order to increase the absorption in lanthanide-doped phosphors, a sensitizer with a sufficient absorption cross-section in the NIR region is usually co-doped along with the emitting ion. Trivalent ytterbium (Yb^{3+}) is the most commonly used sensitizer for UC phosphors. Yb^{3+} has an extremely simple energy level scheme with only one excited 4f level of $^2F_{5/2}$. Moreover, Yb^{3+} has a larger absorption cross-section than any other lanthanide ions, and the absorption band is located at 980 nm. In addition, the $^2F_{7/2}$ $^2F_{5/2}$ transition of Yb^{3+} is well resonant with the transition energy between the $^4I_{11/2}$ and $^4I_{15/2}$ states and also the $^4F_{7/2}$ and $^4I_{11/2}$ states of Er^{3+} ions, thus facilitating the energy transfer from Yb^{3+} to Er^{3+} ions. Usually, a higher concentration of Yb^{3+} sensitizer is doped in UC materials (18–20%). Yb^{3+} is also a standard sensitizer for Tm^{3+} and Ho^{3+} ions.

Lanthanide emitters and sensitizers are generally embedded in a host matrix to fabricate upconversion phosphors. The choice of host matrix has a strong influence on the upconversion process, since the distance between the dopant Ln^{3+} ions, their relative spatial position, their coordination numbers, and the type of anions surrounding the dopant are determined by the host lattice. Halides, such as fluorides, chlorides, bromides, and iodides, and oxides, such as silicates, borates or phosphates, usually serve as hosts to construct upconversion phosphors. Ideal host materials should have low lattice phonon energies and good stability. Generally, halides exhibit low phonon energies but the hygroscopic nature of halides limits their use, whereas oxides are very stable but their phonon energies are relatively higher than 500 cm^{-1}.[27,28] The most promising hosts for upconversion phosphors are found in fluoride materials owing to their low phonon energy (ca. 350 cm^{-1}), high refractive index, and good thermal stability.[29,30]

3. Synthesis of upconversion nanomaterials

3.1. Thermal decomposition

The thermal decomposition method involves the decomposition of organometallic precursors in high boiling point organic solvents in the presence of long alkyl chain surfactants. Decomposition normally takes place at elevated temperatures (300–350 °C). The most frequently used organometallic precursors are metallic trifluoroacetate salts and rare-earth oleates; the solvent is 1-octadecene (ODE); and the surfactants can be oleic acid (OA), oleylamine (OM) or trioctylphosphine oxide (TOPO). The thermolysis method produces high-quality UC nanocrystals with uniform size distribution, high crystallinity and exceptional optical properties.
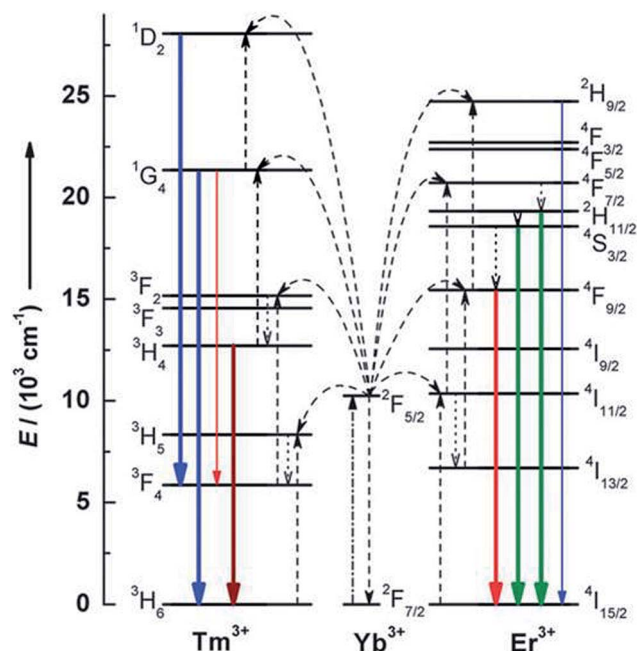

Fig. 3 Proposed energy transfer mechanisms showing the UC processes in Er^{3+}, Tm^{3+}, and Yb^{3+}-doped crystals under 980 nm diode laser excitation. The dashed-dotted, dashed, dotted, and full arrows represent photon excitation, energy transfer, multiphonon relaxation, and emission processes, respectively. Only visible and NIR emissions are shown here. Reproduced from ref. 26 with permission from The Royal Society of Chemistry.

3.1.1. Trifluoroacetate precursors. Yan and co-workers first developed the thermal decomposition method to synthesize highly monodisperse LaF_3 triangular nanoplates from a single-source precursor $La(CF_3COO)_3$ in OA/ODE at 280 °C.[31] This method was later developed as a common route to synthesize other kinds of RE-based NCs. For example, Capobianco and co-workers reported the synthesis of cubic $NaYF_4$ nanoparticles co-doped with Yb/Er or Yb/Tm with broad size distribution (10–60 nm).[32] They further refined the procedure to synthesize nanoparticles with a regular shape and a monodisperse particle size distribution.[33] It was found that slow addition (*ca.* 1 mL min^{-1}) of the precursor solution is the key to synthesize monodisperse nanoparticles. Moreover, Yan and co-workers pioneered the general synthesis of high-quality α/β-$AREF_4$, (A = Na, Li, K and RE = Pr–Lu, Y) NCs *via* the co-thermolysis of $A(CF_3COO)$ and $RE(CF_3COO)_3$ precursors in the mixed solvent of OA-OM-ODE (Fig. 4e–h).[34–36] In this work, pure α-$NaREF_4$ NCs were produced at low temperatures (250–290 °C) and low ratios of Na/RE, while β-$NaREF_4$ NCs were obtained at higher temperatures (330 °C) and high Na/RE ratios. They found that the $\alpha \rightarrow \beta$ phase transition is closely correlated with the particle size. Accordingly, size- and shape-selective synthesis can be carried out by controlling the thermodynamic or kinetic growth of the NCs. Murray and co-workers demonstrated the advantage of the thermal decomposition method by preparing hexagonal $NaYF_4$ nanoparticles in diverse shapes such as spherical NPs, nanorods, hexagonal nanoprisms and nanoplates (Fig. 4i–l).[37] Apart from ODE, oleylamine can also be used as a solvent to prepare UCNPs by the thermolysis method. Chow *et al.* reported the synthesis of small β-$NaYF_4$:Yb,Er nanoparticles in pure oleylamine solvent.[38] In this method, the oleylamine acts as both the solvent as well as the coordinating ligand.

Thermal decomposition

Host	Shape	Size distribution (nm)	Ref.
$NaYF_4$	Sphere, nanorod, nanocube, nanoplate, nanoprism	15–60 narrow	33, 35, 37, 38, 74 and 75
$NaGdF_4$	Sphere	2–30 narrow	35, 57, 76–78
$NaYbF_4$	Sphere, polyhedron	15–60 narrow	35, 60 and 79
$NaScF_4$	Sphere, hexagonal	20–40 narrow	80 and 81
$NaREF_4$ (RE = Nd, Sm, Eu, Tb, Dy, Ho, Er, Tm, Lu)	Sphere, nanorod	10–150	35
$LiREF_4$ (RE = Tb–Lu, Y)	Polyhedron, rhombic nanoplate	20–90 narrow	36
$KREF_4$ (RE = La–Gd, Y)	Nanowire, nanocube and nanopolyhedra	7–20 narrow	36
REF_3 (RE = Y, La, Ce, Pr, Nd, Sm, Eu, Gd, Tb, Dy, Ho, Tm, Yb, Lu)	Nanoplate, sphere, nanozigzag, truncatedoctahedron, nanorod,	5–20 narrow	31, 82 and 83

(*Contd.*)

Thermal decomposition

Host	Shape	Size distribution (nm)	Ref.
MF_2 (M = Mg, Ca, Sr, Ba)	nanopolyhedra rhombic nanodisk Sphere, nanoneedle, nanoplate, nanowire	3–100 narrow	84 and 85
MFCl (M = Ca, Sr, Ba)	Nanocube	12–20 narrow	86
$KMnF_3$	Nanocube	10–40 narrow	87
$NaMnF_3$	Sphere	8–10 narrow	88
RE_2O_3 (RE = Y, Gd)	Nanoplate, nanodisk	5–10 narrow	47–49
YOF	Nanosphere	14–16 narrow	89

The synthesized nanoparticles were uniform in shape, and showed a narrow size distribution (10.5 ± 0.7 nm). Shan *et al.* first reported the use of trioctylphosphine oxide (TOPO) as a replacement for the most frequently used capping agents such as OA and OM.[39–41] The as-synthesized NCs had controllable sizes in the range of 5–20 nm with narrow size distribution. However, they suffer from low solubility in common organic solvents like cyclohexane or chloroform. This problem was later solved by replacing TOPO with trioctylphosphine (TOP) and oleic acid (OA) mixture (TOP/OA).[40,41]

3.1.2. Rare-earth oleate and acetate precursors. Though trifluoroacetate precursors offer many advantages, the release of toxic fluorine species from the thermal decomposition of trifluoroacetates makes them less attractive. Therefore, efforts were made to develop alternative synthetic methods that also allow control over the crystal phase, shape, and size of the particles.

Chen and co-workers reported a non-toxic thermolysis method for the preparation of β-$NaYF_4$ and $NaGdF_4$ NCs. This method involves the reaction of a RE oleate ($RE(OA)_3$) complex and NaF in OA/ODE solvent. By simply changing the ratios of NaF to $RE(OA)_3$, the sizes of the β-$NaYF_4$:Yb,Er/Tm NPs can be tuned from larger nanoplates to smaller nanospheres of size about 18 nm.[42–44] Recently, Na *et al.* controlled the morphology of β-$NaYF_4$:Yb,Er/Tm NPs from large spheres (37.9 nm) to rods (length = 60.1 nm, width = 21.5 nm) and from rods to hexagonal prisms (length = 48.8 nm, width = 44.0 nm).[45] When the OA/ODE ratio was 2 : 19, large spheres (Fig. 5a and b) were produced, whereas nanorods were obtained with a 19 : 2 ratio (Fig. 5c). By adding 2.5 mmol NaCl, the nanorods were transformed to hexagonal prisms (Fig. 5d). The RE oleate method was later extended to synthesize other fluoride NCs, including REF_3 (RE = La–Pr), $NaREF_4$ (RE = Sm–Er), and $Na_5RE_9F_{32}$ (RE = Tm–Lu) with diverse morphologies.[46] In addition to fluoride nanocrystals, $RE(OA)_3$ complexes can also be used to synthesize RE oxide nanostructures.

Tan and co-workers synthesized several doped RE_2O_3 (RE = Y, Gd) nanodots and nanorods by the decomposition of $RE(OA)_3$ precursors in OM solvent (Fig. 5e and f).[47,48] In this method, the first formed nanodots were self-assembled to nanorods with the same diameter by increasing the reaction
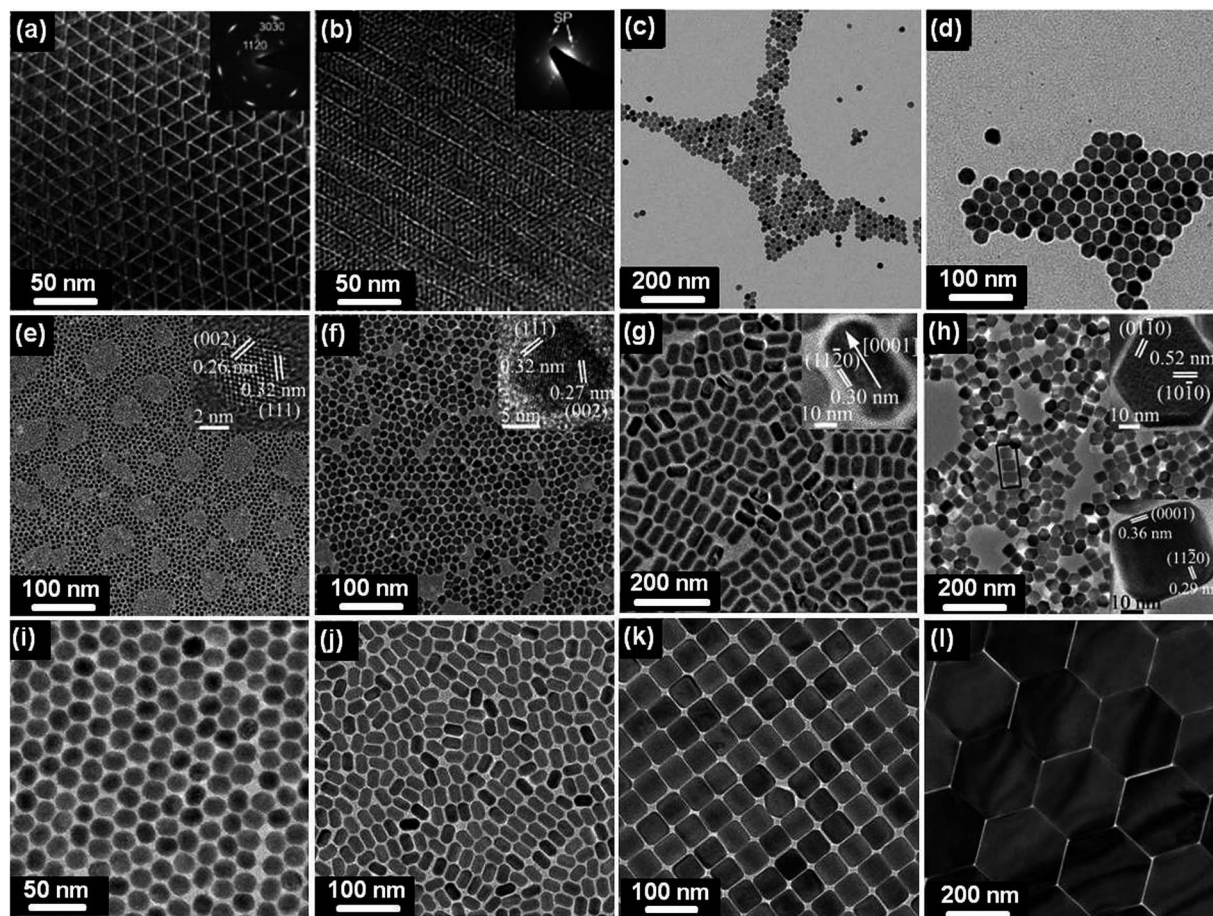
Fig. 4 TEM images of (a and b) LaF₃ nanoplates, (c and d) NaYF₄:Yb,Er nanoparticles, (e) α-NaNdF₄, (f) α-NaYF₄ nanoparticles (g) β-NaYF₄ nanorods, (h) β-NaHoF₄ hexagonal plates. (i–l) TEM images of β-NaYF₄:Yb,Er (i) spherical nanoparticles, (j) nanorods, (k) hexagonal nanoprisms and (l) hexagonal nanoplates. Reprinted with permissions from ref. 31, 33, and 35 (copyrights 2005, 2007, and 2007 American Chemical Society) and ref. 37 (copyright, 2010 National Academy of Sciences).

time from 10 min to 2 h. The self-assembly process was attributed to dipole–dipole interactions. Other RE complex salts, such as acetate (RE(Ac)₃), acetylacetonate (RE(acac)₃), and benzoylacetonate, have been used to synthesis RE oxide nanostructures. Murray and co-workers synthesized tripodal and triangular Gd₂O₃ nanoplates with a thickness of 2 nm using a gadolinium acetate precursor in OA/OM/ODE mixture (Fig. 5g and h).[49] Yan and co-workers explored the preparation of RE oxide nanoplates using RE(acac)₃ and RE benzoylacetonate as precursors.[50,51]

3.1.3. Ostwald ripening strategy. In 2008, Li and Zhang reported a facile and user-friendly method for the synthesis of pure β-NaYF₄ nanocrystals in OA and ODE at 300 °C. In this method, the trifluoroacetate and RE oleate precursors were replaced by RECl₃, and NaOH and NH₄F were used as the Na⁺ and F⁻ sources, respectively.[52] The particles were of high quality in terms of size distribution (average size 21 nm) and shape uniformity (nanospheres and hexagonal plates depending on the amount of oleic acid) (Fig. 5i–l). Two major steps are involved in this method: (1) formation of small amorphous sacrificial NaYF₄ co-precipitates at room temperature, and (2) particle growth *via* the Ostwald ripening mechanism at elevated

temperature (300 °C). To date, a series of monodisperse doped RE fluoride nanoparticles, including NaYF₄,[53–56] NaGdF₄,[57] NaLuF₄,[58] NaDyF₄[59] and NaYbF₄,[60] have been synthesized using this method. Furthermore, this method is well suited for the synthesis of core–shell and core–shell–shell structures with uniform morphology and size by a seeded growth approach. Various core–shell nanostructures, including NaYF₄: Yb,Ln@NaYF₄ (Ln = Er, Tm, Ho),[61–65] NaGdF₄:Yb,Er/ Tm@NaGdF₄,[66] KYF₄:Yb,Er@KYF₄,[67] KGdF₄:Yb,Tm@KGdF₄,[68] NaYF₄:Yb,Er@NaGdF₄,[69–71] NaGdF₄:Yb,Tm@NaYF₄,[62] NaYbF₄: Tm@NaGdF₄,[60] NaYF₄:Yb,Tm@NaYF₄:Yb,Er,[72] as well as core–shell–shell nanostructures, such as NaYF₄:Yb,Tm@NaYF₄: Yb,Tm@NaYF₄ (ref. 73) and NaYF₄:Yb,Tm@NaYF₄: Yb,Er@NaYF₄:Yb,Tm,[72] have been successfully synthesized.

At present, the thermal decomposition and Ostwald ripening methods are becoming the most common methods for the synthesis of high-quality UCNPs. However, some inherent disadvantages still need to be addressed: first, the rigorous and harsh experimental conditions (high temperature, waterless, oxygen-free and inert gas protection); second, the use of expensive solvents and the toxic nature of the by-products from trifluoroacetate; third, the nanoparticles are soluble only in
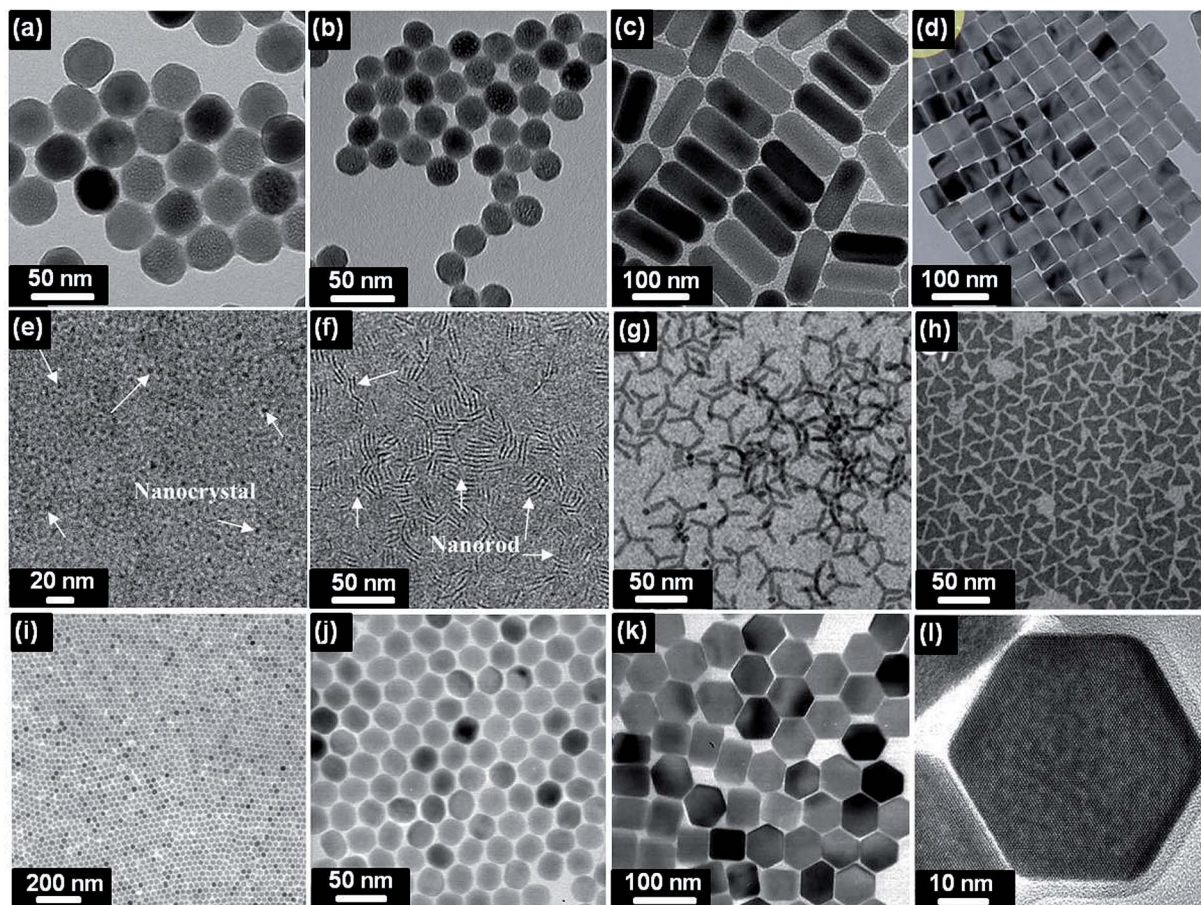
Fig. 5 TEM images of β-NaYF$_4$:Yb,Er (a and b) nanoparticles, (c) nanorods, (d) hexagonal prisms. TEM images of Y$_2$O$_3$:RE nanodots and nanorods obtained at 280 °C after (e) 10 min and (f) 2 h. TEM images of tripodal and triangular Gd$_2$O$_3$ nanoplates synthesized at (g) 280 and (h) 310 °C for 1 h. TEM images of NaYF$_4$:Er,Yb (i and j) nanospheres and (k and l) nanoplates at different magnifications. Reprinted with permissions from ref. 45 (copyright 2013, The Royal Society of Chemistry), ref. 47 and 49 (copyrights 2008, 2013 American Chemical Society), and ref. 52 (copyright 2008, IOP Publishing).

non-polar or weakly polar solvents. Therefore, post-synthesis treatment is needed to make them soluble in common polar solvents such as water and ethanol.

3.2. Hydro(solvo)thermal methods

Hydro(solvo)thermal synthesis utilizes a solvent under pressures and temperatures above its critical point to increase the solubility and reactivity of precursors and allow fine crystallization of the final products. Generally, the reactions are carried out in specialized reaction vessels known as autoclaves, which consist of an inner Teflon liner, an outer stainless steel shell, and a stainless steel cap. The products obtained by the hydro(solvo)thermal method usually exhibit high crystallinity and few defects. Hydro-(solvo)thermal synthesis provides obvious advantages such as (1) higher yield and purity, (2) relatively low reaction temperature (usually below 220 °C) and (3) well-controlled size, structure and morphology of the final product. Based on the reaction conditions hydro(solvo)thermal methods can be broadly divided into three classes: (1) organic additive-free synthesis, (2) hydrophobic ligand-assisted synthesis, and (3) hydrophilic ligand-assisted synthesis.

3.2.1. Organic additive-free hydro(solvo)thermal synthesis. This method provides a straightforward route to synthesize 1D

nanowires, nanorods, and nanotubes without any organic additives and templates. Wang and Li synthesized RE(OH)$_3$ (RE = Y, La, Nd, Sm–Tm) nanowires in a basic solution with NaOH or KOH as precipitant at a hydrothermal temperature of 180 °C.[90,91] They also obtained RE(OH)$_3$ (RE = Y, La–Yb) nanotubes with open ends by lowering the temperature to 120–140 °C.[90,92] Furthermore, RE oxide, oxyfluoride, and oxysulfide nanowires/nanotubes were prepared by calcination, fluoridation, and sulfidation of the as-prepared hydroxide nanowires/nanotubes Zhang and Zhao reported the synthesis of rare-earth fluoride β-NaREF$_4$ nanotubes *via* a hydrothermal *in situ* ion exchange reaction using rare-earth hydroxides [RE(OH)$_3$] as a parent (where RE = Y, Pr, Sm, Gd, Tb, Dy, and Er).[93] In this method, NaF and HF were reacted with RE(OH)$_3$ precursors at 120 °C for 12 h. During this process, HF diffuses into single-crystalline RE(OH)$_3$ nanotubes and F$^-$ ions can substitute for the OH$^-$ ions and interact with RE^{3+} ions to form the more stable β-NaREF$_4$ phase (Fig. 6a and b). Similarly, Xu *et al.* synthesized nearly monodisperse and well-defined one-dimensional (1D) rare-earth fluoride (β-NaREF$_4$) (RE = Y, Sm, Eu, Gd, Tb, Dy, and Ho) nanowires/nanorods (Fig. 6c and d).[94]

3.2.2. Hydrophobic ligand-assisted hydro(solvo)thermal synthesis. In 2005, Li and co-workers developed a facile
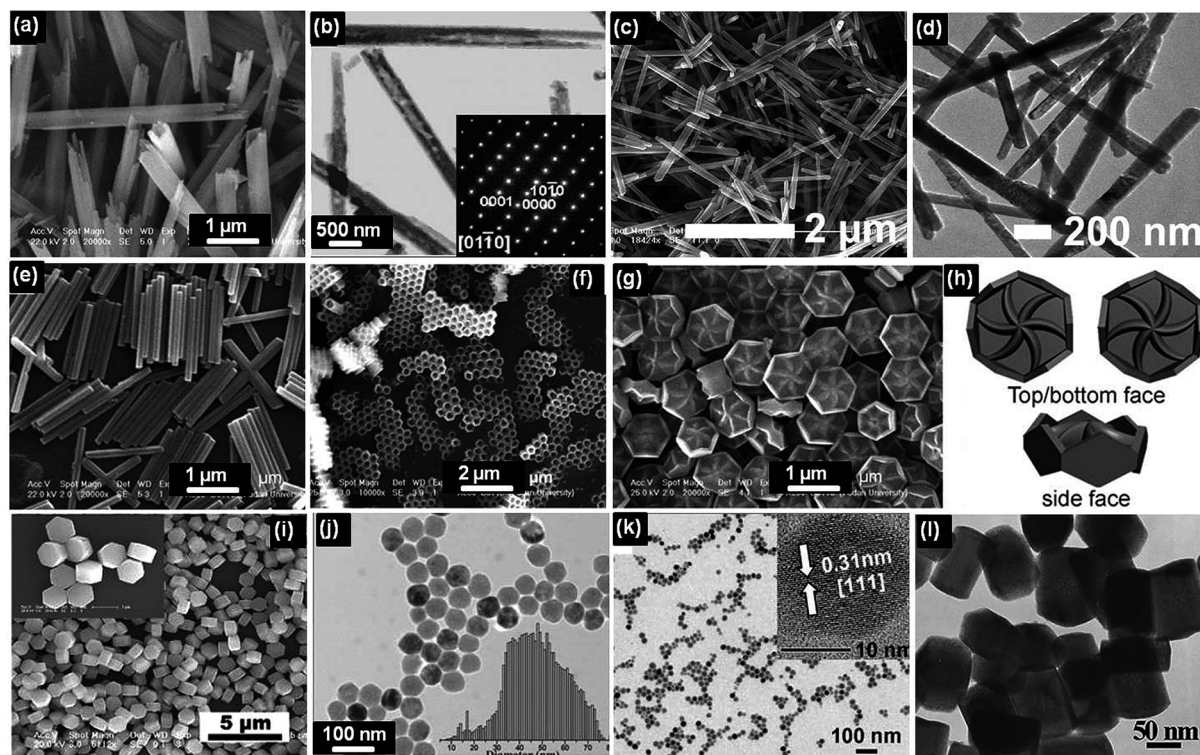
Fig. 6   (a) SEM image of $Y(OH)_3$ nanotubes, (b) TEM image of $NaYF_4$ nanotubes, (c) SEM image of $Y(OH)_3$ nanowires, (d) TEM image of $NaYF_4$ nanowires synthesized using organic additive-free hydro(solvo)thermal synthesis. SEM images of arrays of β-$NaYF_4$ (e) nanorods, (f) nanotubes and (g) flower-patterned hexagonal disks. (h) Illustration of the {0001} top/bottom faces and the {1-100} side faces of a disk. (i) SEM image of β-$NaYF_4$:Tb hexagonal microplates synthesized using Cit^{3-}, (j) TEM image of $BaYF_5$ nanocrystals synthesized using EDTA, (k) TEM image of $NaYF_4$:Yb,Er nanoparticles obtained using PEI and (l) $NaYF_4$:Yb,Er nanocrystals synthesized using PAA. Reprinted with permissions from ref. 93 and 94 (copyright 2008, 2009 American Chemical Society), ref. 99 (copyright 2007, Wiley-VCH Verlag GmbH & Co. KgaA), ref. 109 (Copyright 2007, American Chemical Society), 114 (copyright 2011, The Royal Society of Chemistry), ref. 118 (Copyright 2008, American Chemical Society), and ref. 121 (copyright 2012, The Royal Society of Chemistry).

solvothermal method for preparing hydrophobic NCs using a liquid–solid-solution (LSS) strategy.[95] This method is based on a general phase transfer and separation mechanism occurring at the interfaces of the ethanol–linoleic acid liquid phase (liquid), metal linoleate (solid), and water–ethanol solution containing metal ions (solution). The schematic diagram for the LSS method is illustrated in Fig. 7. In the case of $NaREF_4$ nanocrystal synthesis, the phase transfer process across the solid phase and solution transfers RE^{3+} ions to the solid phase as a RE linoleate $(RCOO)_nRE$ complex. Under designed reaction conditions, the reaction between NaF and $(RCOO)_nRE$ produces $NaREF_4$. Using this method with slight modifications, a variety of UCNPs with well-controlled crystal phase, size, and shape have been synthesized.[96–108] For example, Zhao and co-workers utilized an oleic acid-mediated hydrothermal method for the synthesis of Yb- and Er-doped $NaYF_4$ nanorods, nanotubes, and flower-patterned nano-disks (Fig. 6e–h).[99] Using a similar synthetic system, Liu and co-workers studied the effect of RE^{3+} doping on the crystal phase, size, and optical properties of the $NaYF_4$ UCNPs. They found that RE^{3+} doping at precisely defined concentrations, controlled the sizes (down to 10 nm), phases (cubic or hexagonal), and UC emission colors (green to blue).[102] Recently, Tian et al. used an LSS method to synthesize Mn^{2+}-
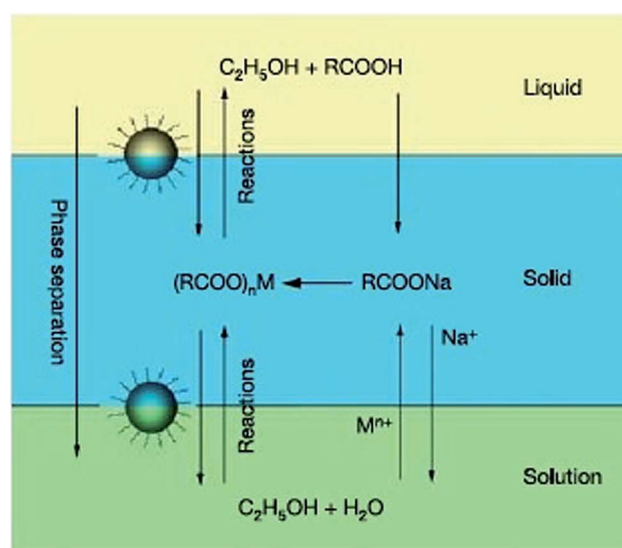

Fig. 7   Scheme of liquid–solid–solution (LSS) phase transfer synthetic strategy. Adapted from ref. 95. Copyright 2005, Nature Publishing Group.

doped $NaYF_4$:Yb,Er UCNPs. It was found that without Mn^{2+} ions, the synthesized nanoparticles were mixed-phase (hexagonal and cubic) and had two different morphologies that included small nanocubes (cubic phase) and larger hexagonal nanorods (hexagonal phase). When 30 mol% Mn^{2+} ions were doped, single cubic phase and smaller (~20 nm) $NaYF_4$:Yb,Er nanoparticles were obtained.[105]

3.2.3. Hydrophilic ligand-assisted hydro(solvo)thermal synthesis. Water-soluble UCNPs can be prepared using hydrophilic ligands such as citrate (Cit^{3-}),[109–112] ethylenediaminetetraacetic acid (EDTA),[113,114] polyvinyl pyrrolidone (PVP),[115] cetyltrimethylammonium bromide (CTAB),[116] poly-(ethyleneimine) (PEI),[117–120] and poly(acrylic acid) (PAA).[121,122] Polydentate Cit^{3-} is considered as one of the most important chelating and structure-directing agents in upconversion phosphor synthesis. Lin and co-workers systematically studied the effect of various factors such as the amount of Cit^{3-}, pH value, and fluoride source in tailoring the crystal phases, shapes, and sizes of $NaREF_4$ (RE = Y, Yb, Gd, and Lu) nano/microcrystals.[109–111] The products obtained using Cit^{3-} are often plate-like microcrystals. EDTA and Na_2EDTA (ethylenediaminetetraacetic acid disodium) are other polydentate organic additives that have a similar structure-directing function as Cit^{3-}. Recently, Qiu et al. synthesized Yb- and Er-doped $BaYF_5$ nanoparticles using EDTA in a hydrothermal method.[114] They showed that the size of the $BaYF_5$ nanocrystals can be controlled by the slow release of Ba^{2+} from the chelating complex Ba–EDTA and reducing the pH levels. Apart from Cit^{3-} and EDTA, polymeric organic compounds with $-NH_2$ and $-COOH$ groups are also used to synthesize water-soluble UCNPs. Wang et al. first reported the synthesis of PEI-coated $NaYF_4$:Yb,Er/Tm NPs with an average particle size of 50 nm in ethanol solution. They also demonstrated that the high molecular weight of PEI is more efficient for controlling the particle growth and stabilizing the particles against aggregation.[117] Later, they prepared monodisperse $NaYF_4$:Yb,Er/Tm nanoparticles of size 20 nm in an ethylene glycol medium.[118] Li and co-workers reported the synthesis of β-$NaYF_4$:Yb,Er/Tm nanorods using PAA as surfactant in a facile solvothermal method.[121]

3.3. Other methods

In addition to these widely used methods, there are many other methods, such as co-precipitation, microwave-assisted methods, and ionic-liquid-based synthesis, which possess attractive advantages and have been employed to produce UCNPs.

3.3.1. Co-precipitation. Co-precipitation is one of the earliest and most convenient techniques for synthesizing UCNPs. Sub-10 nm REF_3 (RE = Eu, Er, Nd, Ho) NPs were prepared by van Veggel and co-workers, through the co-precipitation of RE^{3+} and F^- ions assisted by ammonium di-*n*-octadecyldithiophosphate in an ethanol-water solution at a low temperature of 75 °C.[135] Yi et al. synthesized $NaYF_4$:Yb,Er NPs by a co-precipitation method in the presence of EDTA.[136] They controlled the particle size in the range of 37–166 nm by changing the molar ratio of EDTA to RE^{3+} ions. The as-prepared

nanoparticles emit very weak upconversion fluorescence; however, when annealed at temperatures between 400 and 600 °C the emission intensities were enhanced 40-fold. This is attributed to the phase transition from cubic to hexagonal. Unfortunately, the NPs lost their spherical shape and aggregated after heating. Recently, He et al. synthesized Yb^{3+}- and Er^{3+}/Tm^{3+}/Ho^{3+}-co-doped β-$NaGdF_4$ microstructures in the presence of Na_2EDTA, PVP, sodium dodecyl sulfonate (SDS), and sodium tartrate (Na_2tar).[137] In their method, the surfactants play an important role in controlling the size, morphology, upconversion luminescence and magnetic properties of the microstructures. Even though the co-precipitation method is simple, post-heat treatment (annealing) is often required to enhance UC fluorescence intensity, which in turn allows the NPs to aggregate and become larger. After annealing, organic capping reagents, such as EDTA and PVP, will be carbonized, which reduces the hydrophilicity of the products.

3.3.2. Microwave-assisted synthesis. In the last few years, microwave-assisted methods have aroused considerable attention in the synthesis of UCNPs. Microwave heating offers many advantages over conventional heating such as higher heating rates, uniform heating throughout the sample, reduced reaction times, reduction in unwanted side reactions, higher yields and improved reproducibility.[141] Wang et al. synthesised oleic acid-capped cubic $NaYF_4$ and $Na_xLi_yYF_4$ nanocrystals by a facile microwave irradiation method. In this method, the reaction time was significantly reduced to 5 min and the synthesized nanoparticles were monodisperse and highly luminescent.[142] Mi et al. prepared highly crystalline, strongly luminescent $NaYF_4$:Yb,Er UCNPs in ethylene glycol at a lower temperature (160 °C) and shortened reaction time (only 1 h).[143] However, the crystalline phase of the as-prepared nanoparticles was a mixture of both α and β. Later, Yang and co-workers investigated the effect of various reaction parameters on the formation of phase-pure $NaYF_4$:Yb,Er.[144] They demonstrated that by increasing the NH_4F content in the ethylene glycol (EG) solvent, the phase of the as-prepared nanoparticles can be gradually transformed from cubic to hexagonal.

3.3.3. Ionic liquid-assisted synthesis. In recent years, ionic liquids have emerged as one of the most promising categories of medium for the synthesis of nanomaterials due to their exceptional features, such as negligible vapour pressure, good thermal and chemical stability, relatively low viscosity, extremely high ionic conductivity, and wide electrochemical windows.[147,148] In addition, ionic liquids have superior capability for the dissolution and stabilization of metal cations, which gives them the possibility of acting as solvents, capping agents, or surfactants in inorganic synthesis. Zhang and co-workers reported the ionothermal synthesis of $NaYF_4$:Yb,Er/Tm UCNPs using 1-butyl-3-methylimidazolium tetrafluoroborate [Bmim][BF_4].[149] In this method, the ionic liquid [Bmim][BF_4] acts as both solvent and F^- source as well as template, which facilitates the formation of small hexagonal-phase products. Ionic liquids are excellent absorbers of microwaves; hence, they are used as solvents and F^- sources in microwave heating methods. This method significantly reduces

the reaction time (5–20 min) and produces highly crystallized products.[150]

3.3.4. Gas-phase synthesis methods. Glaspell *et al.* reported the synthesis of Y_2O_3 nanocrystals doped with Yb^{3+}, Er^{3+}, and Ho^{3+} using a vapor-phase synthesis approach based on the laser vaporization/controlled condensation (LVCC) technique.[151] This method combines the features of pulsed laser vaporization of the target materials with a controlled condensation process from the vapor phase. This method produces highly crystalline upconversion nanocrystals; therefore, it eliminates the post-annealing process typically required for some other methods. Gas-phase flame synthesis is another promising technique since it can produce high-purity nanocrystals with small primary sizes in a single-step process. Qin *et al.* synthesized Yb^{3+}- and Er^{3+}-doped Y_2O_3 nanoparticles in two different sizes (27 and 14 nm) by controlling the flame temperature.[152] Kong *et al.* reported the flame synthesis of Yb^{3+}/Er^{3+} co-doped into Y_2O_3, La_2O_3, and Gd_2O_3 nanoparticles. The average sizes of the particles were around 50 nm.[153]

3.4. Upconversion photoluminescence measurements

A typical setup for upconversion photoluminescence measurement is shown in Fig. 8.[154] In this setup, a fiber-coupled 980 nm laser is used as the excitation source for the upconversion excitation. A laser adapter and a beam collimator are used to guide the laser into the sample holder. The upconversion emission spectrum is recorded using a monochromator equipped with a photon-counting photomultiplier. The excitation and detection chambers are operated using a 90° measurement geometry in order to avoid the entrance of the excitation laser into the detector.

The measurement of the absolute quantum yield (QY) of upconversion phosphors has been a difficult task. Page *et al.* pioneered the determination of the absolute quantum yield of bulk UC phosphors. The calculated QY was 4% for the green emission of Yb^{3+},Er^{3+}-doped hexagonal $NaYF_4$.[155] Van Veggel *et al.* reported a technique for measuring QYs of upconverting nanomaterials based on the use of a commercially available fluorimeter and an integrating sphere. By using this setup, they calculated the QY of colloidal β-$NaYF_4$:Yb^{3+},Er^{3+} nanoparticles. The values were in the range of 0.005–0.3%, depending on the particle size.[156]

4. Upconversion luminescence enhancement

The synthesis of highly luminescent UCNPs is very important for considering the application of these NPs in solar cells and other fields. There are several strategies available to enhance the upconversion luminescence such as (1) impurity doping, (2) plasmonic enhancement and (3) construction of core–shell nanostructures.

4.1. Impurity doping

It is well known that the upconversion luminescence intensities of lanthanide ions are mainly dependent on electronic transition probabilities, which are highly sensitive to the surrounding environment of the Ln^{3+} ions. Consequently, tailoring the local crystal field of the Ln^{3+} ions could be an effective strategy to increase the UC emissions of various host materials doped with lanthanide ions. The crystal symmetry in UC nanocrystals can be altered by an intentional doping of non-luminescent cations. Fig. 9 shows the possible changes in the crystal lattice after impurity doping. For homo-valence ion doping, depending on the size of the impurity dopants, the host lattice will contract (smaller dopants) or expand (larger dopants). hetero-valence ion doping is always accompanied by formation of vacancy sites or an extra ion occupying the interstitial site. In addition, it is also possible to dope the impurities directly into the interstitial positions.[157] One of the most successful impurity ions is Li^+.
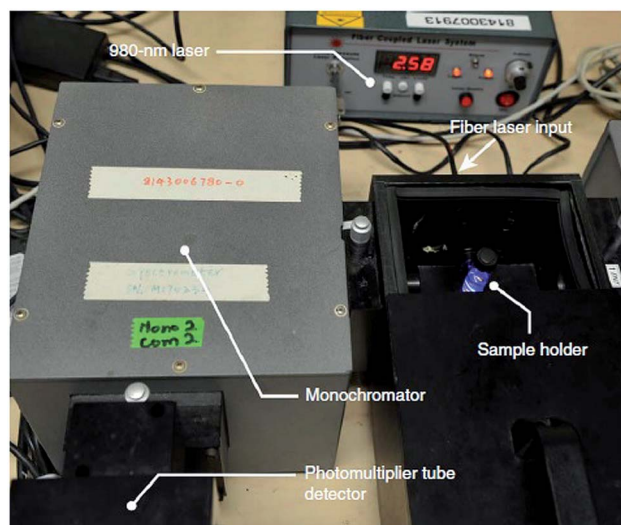

Fig. 8 Photograph of the experimental setup for the measurement of upconversion emission spectra. Adapted from ref. 154. Copyright 2014, Nature Publishing Group.
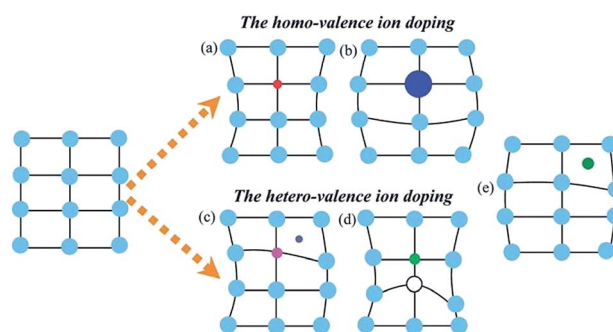

Fig. 9 Schematic illustration of the possible impurity doping routes in the host lattice: (a) substitution by a small homo-valence dopant, (b) substitution by a large homo-valence dopant, (c) combination of substitution by a hetero-valence dopant and interstitial occupation by an extra ion for charge compensation, (d) combination of substitution by a hetero-valence dopant and vacancy occupation for charge compensation, and (e) interstitial occupation by a small dopant. Adapted from ref. 157. Copyright 2013, The Royal Society of Chemistry.

Due to its small ionic radius, Li^+ ion can be doped easily into the host lattice substitutionally or interstitially. This will result in alteration of the crystal field around the rare-earth ions, leading to enhanced upconversion PL intensity. Li^+ doping was found to be highly successful in oxide UCNPs with varying host lattice and lanthanide dopants.[158–160] For example, Zhang and co-workers observed a 25-fold enhancement of the visible UC emissions in Li^+-co-doped Y_2O_3:Yb,Er NPs.[158] Recent reports show that Li^+ doping can also produce the same results in fluoride host materials such as $NaYF_4$:Yb,Er/Tm.[142,161–163] In addition to Li^+, other cations such as Bi^{3+}, Fe^{3+}, Sc^{3+}, and Ca^{2+} can also be used to tailor the local crystal symmetry.[57,144,164,165] For example, Huang et al. observed enhanced upconversion emissions in hexagonal $NaYF_4$ by tridoping the structure with Sc^{3+}, Er^{3+}, and Yb^{3+}.[164] They systematically studied the change in the crystal symmetry of $NaYF_4$:Yb,Er by Sc^{3+} doping, using X-ray diffraction (XRD), X-ray photoelectron spectroscopy (XPS), and decay time investigations. Our group recently observed fluorescence enhancement in Fe^{3+}-doped $NaGdF_4$:Yb,Er nanocrystals.[57] In 30 mol% Fe^{3+}-doped samples, the green and red UC emissions were enhanced by 34 and 30 times, respectively (Fig. 10).

4.2. Plasmonic enhancement

Localised surface plasmon resonance (LSPR) from noble metal nanostructures can be used to enhance upconversion luminescence. There are three different methods usually followed to enhance UC emissions using plasmonic nanostructures. (1) Deposition of upconversion nanoparticles on metallic nanostructure films. UC nanoparticles have been deposited over a variety of metallic films such as gold islands,[166] dense metal nanoparticles (Ag or Au),[167,168] 3D plasmonic antenna,[169] Au nanohole arrays,[170] and gold pyramid arrays.[171] Zhang et al. observed five-fold overall enhancement of upconversion emissions in $NaYF_4$:Yb,Er nanocrystals when coupled with gold island films.[166] The upconversion enhancement is highly dependent on the distance between the upconverters and the metallic structures. Saboktakin et al. proposed a new configuration in which close-packed monolayers of UCNPs are separated from a dense multilayer of metal NPs (Au or Ag) by nanometer-scale aluminium oxide grown by atomic layer deposition (Fig. 11). The spacer layer thickness varied from 2 to 15 nm. They observed 45-fold enhancement for $NaYF_4$:Yb,Er nanoparticles over Ag nanoparticle films separated by 10 nm Al_2O_3.[168] Recently, the same group reported 35-fold enhancement in the upconversion luminescence of $NaYF_4$:Yb,Er in Au nanohole arrays.[170] The enhancements were mainly due to the combined effects of an enhancement in the excitation of sensitizers and an increase in the radiative decay rate of emitters. (2) In the second approach, metal nanoparticles or nanoshells are formed on the surface of UCNPs. Zhang et al. studied the effect of gold nanoparticles or nanoshells on the UC emissions of $NaYF_4$:Yb,Tm hexagonal nanoplates.[172] Attachment of gold nanoparticles enhanced the upconversion by a factor of 2.5, whereas the growth of nanoshells quenched the UC emissions by a factor of 3 to 4. Li et al. also observed the same phenomenon in $NaYF_4$:Yb,Er,Gd nanorods.[173] It was proposed that the gold shell on the UCNPs can significantly scatter the excitation light at 980 nm and reduces the excitation flux. In addition, the complete surrounding gold shell can also block the emission transmittance from the UCNPs. (3) The third approach is by forming a core–shell structure of metal NPs–silica–UCNPs or UCNPs–silica–metal NPs. This method allows one to precisely control the distance between UCNPs and metal NPs. Various core–shell structures, such as $NaYF_4$:Yb,Er@SiO_2@Ag, $NaYF_4$:Yb,Er@SiO_2@Au, and Ag@SiO_2@Y_2O_3:Er, have been developed to enhance UC luminescence.[174–176] Yuan et al. observed 14.4-fold enhancement in $NaYF_4$:Yb,Er@SiO_2@Ag core–shell nanostructures with 10 nm SiO_2 shell thickness. They also found that the use of different-sized Ag NPs resulted in different enhancement factors (14.4 times for 15 nm and 9.5 times for 30 nm Ag NPs).[174]

4.3. Core–shell nanostructures

Construction of core–shell structures has become an important strategy in UC nanomaterial synthesis to improve the emissions of UCNPs. The shell enhances the photoluminescence by protecting the luminescent ions in the core from non-radiative decay caused by the surface defects, as well as from vibrational deactivation ascribed to solvent molecules and ligands absorbed on the NC surface. Commonly, core–shell structures can be classified into two types. In type 1, the active Ln^{3+}-doped core is covered with an undoped inert shell such as $NaYF_4$:Yb,Er@$NaYF_4$ and $NaYF_4$:Yb,Er@$NaGdF_4$.[61–71] Yi et al. reported that the visible UC emissions in hexagonal-phase $NaYF_4$:Yb,Er and $NaYF_4$:Yb,Tm were enhanced by 7.4 times and 29.6 times, respectively, by growth of a thin layer of $NaYF_4$ (~2 nm).[177] In addition to rare-earth fluoride shells, CaF_2 has also been explored as an efficient heterogeneous shell material to enhance upconversion emissions. Wang et al. reported ~300-fold enhancement of UC emission yield in 10–13 nm $NaYF_4$:Yb,Er@CaF_2 core–shell nanoparticles in comparison to the core $NaYF_4$:Yb,Er nanoparticles.[178] In the second type of core–shell structures, the shell material is also doped with lanthanide ions (Fig. 12a).

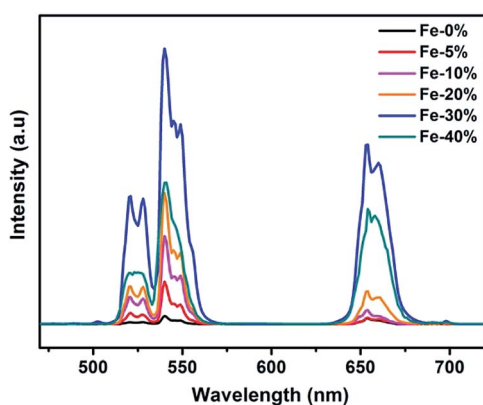**Fig. 10** UC luminescence spectra of $NaGdF_4$:Yb,Er,Fe (0–40 mol%) nanoparticles under 980 nm excitation at room temperature. Reproduced from ref. 57. Copyright 2013, The Royal Society of Chemistry.
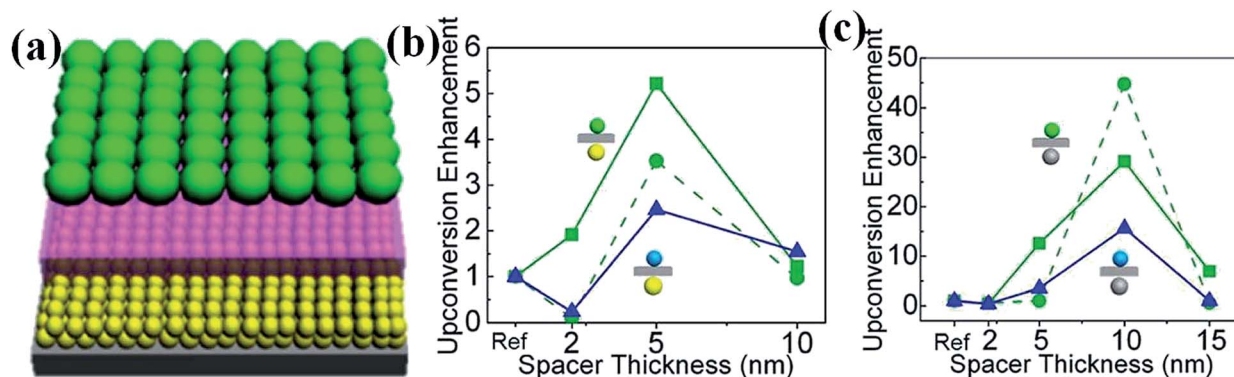
Fig. 11 (a) Schematic structure of a spin-cast layer of Au or Ag NPs, a thin Al_2O_3 layer, and a monolayer of UCNPs. Integrated area under the upconversion emission peak as a function of the Al_2O_3 layer thickness normalized to that of the pure UCNP sample for (b) Au NPs and (c) Ag NPs. The green solid lines correspond to the 540 nm emission band (510–570 nm) in $NaYF_4$:Yb, Er. The green dashed lines correspond to the 650 nm emission band (640–680 nm) in $NaYF_4$:Yb,Er. The blue solid lines correspond to the 475 nm emission band (461–490 nm) in $NaYF_4$:Yb,Tm. Reprinted with permission from ref. 168 Copyright 2012, American Chemical Society.
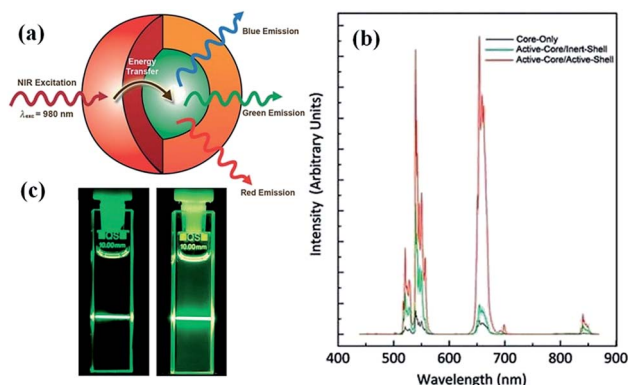

Fig. 12 (a) General depiction of the active-core/active-shell nanoparticle architecture showing the absorption of NIR light by the Yb^{3+}-rich shell (represented in red) and subsequent energy transfer to the Yb,Er-*co*-doped core (represented in green), which leads to upconverted blue, green, and red emissions. (b) Upconversion luminescence spectra of colloidal core–shell nanoparticles. (c) Photographs of colloidal solutions of (A) $NaGdF_4$:Yb,Er active-core/$NaGdF_4$ inert-shell nanoparticles and (B) active-core/active-shell $NaGdF_4$:Yb,Er/$NaGdF_4$:Yb nanoparticles in toluene (1 wt%) following excitation with 980 nm light. Reprinted with permission from ref. 179. Copyright 2009, WILEY-VCH Verlag GmbH & Co. KGaA, Weinheim.

In this type, the Ln^{3+} ions in the shell further enhance the UC emission by interacting with the Ln^{3+} dopants in the core nanoparticles. Capobianco *et al.* reported the synthesis of $NaGdF_4$:Yb,Er active-core@$NaGdF_4$:Yb active-shell nanoparticles and observed enhanced upconversion emissions compared to either the $NaGdF_4$:Yb,Er active-core@$NaGdF_4$ inert-shell or the $NaGdF_4$:Yb,Er core-only nanoparticles.[179] The Yb^{3+} ions in the active shell can harvest more NIR light and transfer it to the core. Wang *et al.* synthesized a series of $NaGdF_4$:Yb,Tm@$NaGdF_4$:Ln (Ln = Eu, Tb, Dy, Sm) NPs. They realized tunable UC emissions for Eu^{3+}, Tb^{3+}, Dy^{3+}, and Sm^{3+} ions by taking advantage of energy transfer processes from sensitizer Yb^{3+} to accumulator Tm^{3+}, then to migrator Gd^{3+}, and

finally to activator Ln^{3+} ions. Making use of this structure, the colour of Eu^{3+}-doped samples can be tuned from blue to red by changing the Eu^{3+} concentration from 0 to 15 mol% in the shell.[180]

5. Solar cell application

Gibart *et al.* first reported the application of upconversion phosphors for improving the performance of solar cells in 1996. They combined the GaAs solar cell with a vitroceramic material doped with Yb^{3+} and Er^{3+} and obtained an efficiency of 2.5% under high excitation densities.[181] Since then, many research groups have been involved in the development of upconversion-based solar cells. Upconversion materials singly doped with Er^{3+} or Ho^{3+} are highly suitable for narrow band gap c-Si solar cells (E_g = 1.12 eV; 1100 nm), since they can convert long-wavelength (~1500 nm) NIR light into short-wavelength (980, 800, 660, 550 nm) NIR and visible emissions. For other solar cell types, such as amorphous silicon (a-Si), DSSC, and organic solar cells, the utilization of Yb^{3+} co-doped with Er^{3+} or Ho^{3+} upconversion materials is very convenient due to efficient ETU from the Yb^{3+} sensitizer to the activators (Table 2).

5.1. Upconversion for c-Si solar cells

Er^{3+}-doped upconversion materials are widely used for c-Si solar cells due to the GSA of Er^{3+} being in the range of 1480–1580 nm ($^4I_{15/2}$–$^4I_{13/2}$ transition). When absorbing a certain number of photons with wavelength of about 1500 nm, the Er^{3+} ion produces four upconversion emission bands: $^4I_{11/2}$–$^4I_{15/2}$, 980 nm; $^4I_{9/2}$–$^4I_{15/2}$, 810 nm; $^4F_{9/2}$–$^4I_{15/2}$, 660 nm; and $^4S_{3/2}$–$^4I_{15/2}$, 550 nm (Fig. 13).[176] These emission bands are well matched with the absorption region of c-Si. Shalav *et al.* used an Er^{3+}-doped $NaYF_4$ upconversion phosphor to enhance the responsivity of a silicon solar cell in the NIR. The phosphors were mixed into an optically transparent acrylic adhesive medium and attached to the rear side of a bifacial silicon solar cell. An external quantum efficiency of 2.5% was obtained for the solar cell under

Table 2 Selected lanthanide-doped upconversion materials used for solar cell applications

| Dopant ion	Host lattice	Excitation (nm)	Emission (nm)	Solar cell type	Ref.
Er^{3+}	$NaYF_4$	1523	550, 660, 800, 980	c-Si	182 and 183
Er^{3+}	CaF_2	1550	660, 980	c-Si	184
Er^{3+}	$Gd_2(MoO_4)_3$	1530	545, 665, 800, 980	c-Si	185
Er^{3+}	$NaGdF_4$	1530	527, 540, 653	c-Si	186
Er^{3+}	Y_2O_3	1538	562, 659, 801, 987	c-Si	187
Er^{3+}	Gd_2O_2S	1510	540, 660, 820, 990	c-Si	188
Er^{3+}	Fluoride glass	1532	550, 660, 820, 980	c-Si	189
Er^{3+}	BaY_2F_8	1557	540, 670, 800, 970	c-Si	190
Yb^{3+}, Er^{3+}, In^{3+}	$LiNbO_3$	1550, 980	530, 558, 672	c-Si/a-Si	191
Ho^{3+}	Glass ceramics containing PbF_2 nanocrystals	1170	650, 910	c-Si	192
Yb^{3+}, Ho^{3+}	Fluoroindate glass	1155	550, 650, 750, 905, 980	c-Si	193
Yb^{3+}, Er^{3+}	$NaYF_4$	980	525, 540, 640–660	a-Si	195–197
Yb^{3+}, Er^{3+}, Gd^{3+}	$NaYF_4$	980	540, 660	a-Si	198
Yb^{3+}, Er^{3+}	Glass ceramic containing $NaYF_4$ nanocrystals	980	520, 538, 656	a-Si	199
Er^{3+}	$NaYF_4$	1560, 980	540, 650, 803, 980	a-Si	200
Yb^{3+}, Er^{3+}	Gd_2O_2S	980	510–560, 650–680	a-Si	201
Yb^{3+}, Er^{3+}	LaF_3	980	543, 655	DSSC	205
Yb^{3+}, Er^{3+}	YF_3	980	525, 545, 656	DSSC	206
Yb^{3+}, Er^{3+}	$NaYF_4$	980	520–570, 650–700	DSSC	207–217
Yb^{3+}, Er^{3+}, Fe^{3+}	$NaGdF_4$	980	525, 540, 653	DSSC	218
Yb^{3+}, Er^{3+}	$Na(Y_{1.5}Na_{0.5})F_6$	980	540, 660	DSSC	219
Er^{3+}	Y_2O_3	980	560, 660	DSSC	220
Yb^{3+}, Er^{3+}	Gd_2O_3	980	564, 650–700	DSSC	221
Yb^{3+}, Er^{3+}	$Y_3Al_5O_{12}$	980	563, 677	DSSC	222
Yb^{3+}, Er^{3+}	TiO_2	980	533, 547, 658	DSSC	223 and 224
Er^{3+}	TiO_2	980	439, 488, 536, 565, 664	DSSC	225
Yb^{3+}, Tm^{3+}	Lu_2O_3	980	476, 653	DSSC	226
Yb^{3+}, Er^{3+}	YF_3	975	540, 660	Organic	227
Yb^{3+}, Er^{3+}	MoO_3	975	520–540	Organic	228
Yb^{3+}, Er^{3+}	$NaYF_4$	980	540, 660	Organic	229 and 231
Yb^{3+}, Ho^{3+}	Y_2BaZnO_5	986	545, 660, 780	Organic	230
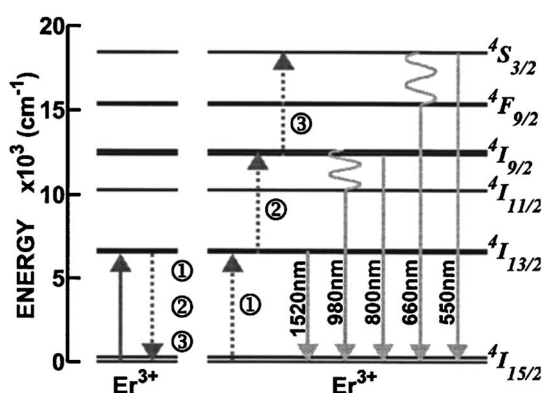
Fig. 13 Three-step UC process between two erbium (Er^{3+}) ions. Energy relaxation from one Er^{3+} ion (sensitizer) can result in energy transfer to a neighboring Er^{3+} ion (activator), giving rise to higher-energy photons. Solid lines represent photon absorption (up) and emission (down), dotted lines represent energy transfer, and wavy lines represent phonon emission. For the two-step process, photons with energies greater than the band gap of silicon are emitted. Reproduced with permission from ref. 182. Copyright 2005, American Institute of Physics.

excitation at 1523 nm with a 5.1 mW laser.[182] Fischer and co-workers also investigated the application of Er^{3+}-doped $NaYF_4$ to enhance the conversion efficiency of c-Si solar cells. The UC efficiency of $NaYF_4$:Er^{3+} phosphor was determined to be 5.1% at a monochromatic irradiance of 1880 W m^{-2} at 1523 nm. The c-Si solar cell with the upconversion phosphor produced an external quantum efficiency of 0.34% at an irradiance of 1090 W m^{-2} at 1522 nm.[183] Liang *et al.* proposed $Gd_2(MoO_4)_3$:Er^{3+} nanophosphors as potential luminescent materials to enhance the response of the silicon solar-cell in the NIR region. Upon excitation with low-energy, near-infrared photons, the phosphor produced intense upconverted emissions at 545, 665, 800, and 980 nm with efficiencies of 0.12%, 0.05%, 0.83%, and 1.35%, respectively.[185] Recently, Meijerink and co-workers investigated the luminescence properties of Er^{3+}-doped Gd_2O_2S for solar cell applications. UC emission and quantum yield measurements showed that Gd_2O_2S doped with 10% Er^{3+} has an internal UC quantum yield of 12.0% $\pm$ 1.0% under monochromatic excitation around 1500 nm at a power of 700 W m^{-2}. This value is higher than the well-known Er^{3+}-doped β-$NaYF_4$ (8.9% $\pm$ 0.7%).[188]

In addition to the Er^{3+} ion, Ho^{3+}-doped UC phosphors have also been explored to enhance the performance of c-Si solar cells. Lahoz, in 2008, used Ho^{3+}-doped oxyfluoride glass

ceramics as promising upconverters for efficiency enhancement in c-Si solar cells. The Ho^{3+} ion has a relatively wide absorption band in the 1150–1225 nm spectral range due to the $^5I_8$–$^5I_6$ transition. When excited at 1170 nm, the Ho^{3+} ion emits two upconverted emissions in the visible ($\sim$650 nm, $^5F_5$–$^5I_8$ transition) and NIR ($\sim$910 nm, $^5I_5$–$^5I_8$ transition) spectral ranges via an ETU mechanism.[192] Later, Lahoz et al. co-doped Ho^{3+} with Yb^{3+} in fluoroindate glass and observed enhanced upconversion efficiency as a function of Yb^{3+} concentration. Because of the high transparency around 1540 nm of Ho^{3+}-doped phosphors, the authors proposed a double-layer structure of Ho^{3+}-doped material together with Er^{3+}-doped material to take advantage of the UC potential of both types of materials.[193]

Recently, Cheng et al. proposed a core–shell structure to extend the NIR wavelength range excitable for upconversion emissions. The authors synthesized NaGdF$_4$:Er^{3+}@NaGdF$_4$: Ho^{3+}@NaGdF$_4$ core–shell–shell nanoparticles and investigated their upconversion properties. In these NCs, the intermediate shell enhances the UC luminescence of Er^{3+} in the core by a passivation mechanism, as well as acting as the host to realize the UC luminescence of Ho^{3+}. More importantly, the upconversion quenching of Er^{3+} and Ho^{3+} was effectively suppressed by doping Er^{3+} and Ho^{3+} in the nanoparticle core and shell, respectively. As a result, intense upconversion emissions for both Er^{3+} and Ho^{3+} dopants were achieved.[194]

5.2. Upconversion for amorphous silicon solar cells

Compared with crystalline silicon, amorphous silicon has a band gap of $\sim$1.75 eV and can only absorb light of wavelength shorter than 708 nm. In order to utilize NIR light in amorphous Si solar cells, Yb^{3+} co-doped with Er^{3+} or Ho^{3+} upconversion materials can be used. Zhang and co-workers, synthesized NaYF$_4$:Yb,Er nanoparticles using an EDTA-assisted hydrothermal method. An upconverter layer was fabricated, by mixing the phosphor with polydimethylsiloxane (PDMS), and attached to the rear side of the solar cell. The short-circuit current density of the device was increased from 15.99 to 17 mA cm^{-2}.[195] Wild et al. mixed the upconversion NaYF$_4$:Yb,Er phosphor with polymethylmethacrylate, and then made it into an upconverter layer with thickness of 200–300 μm. A maximum current enhancement of 10 μA was measured on illumination with a 980 nm diode laser at 10 mW.[196,197] Li et al. prepared gold nanostructure-decorated NaYF$_4$:Yb,Er,Gd nanorods and applied them in a-Si solar cells. The authors obtained a 72-fold improvement in the short-circuit current and a maximum current of 1.16 mA for the cell using UC nanorods coated with Au nanoparticles under 980 nm laser illumination.[198] Recently, Wild et al. showed the upconversion photoresponse in a-Si solar cells with broadband light excitation using a Gd$_2$O$_2$S:Yb^{3+},Er^{3+} upconverter. The authors made a setup to concentrate near-infrared light (longer than 900 nm) from a solar simulator up to 25 times. The photoresponse obtained from broadband excitation was the same as that under laser light excitation.[201]

5.3. Upconversion for dye-sensitized solar cells

Dye-sensitized solar cells have attracted increasing attention in the solar energy conversion sector due to their low cost, easy fabrication, and high efficiencies. Unlike Si solar cells, a typical DSSC consists of a dye-sensitized nanocrystalline TiO$_2$ semiconductor film on transparent conductive oxide (TCO) glass, an electrolyte solution containing a I$^-$/I$_3^-$ redox couple, and a platinum-coated TCO glass as a counter electrode. Upon excitation, the dye molecules absorb photons and inject electrons into the conduction band of TiO$_2$ from the excited state of the dye. The dye ground state is regenerated by electron transfer from a redox species in solution, which is then reduced at the counter electrode. By great efforts of researchers, DSSCs have reached an efficiency of 13%.[202] However, this conversion efficiency is still not enough for commercialization. A major factor limiting the performance of DSSCs is the incapacity of utilizing near-infrared (NIR) and infrared (IR) photons. The most commonly used sensitizers such as N3, N719, and N749 can absorb light with wavelengths in a range between 300 and 800 nm due to their large band gap $\sim$1.8 eV.[203,204] DSSCs can effectively utilize NIR light with the aid of upconversion emission from UCNPs. Fig. 14 shows the absorption spectrum of the N719 dye and the UC emission spectrum of β-NaYF$_4$:Yb,Er nanoparticles. The absorption peak of the N719 dye is resonant with the green emission ($\sim$550 nm) of the UCNPs. As a

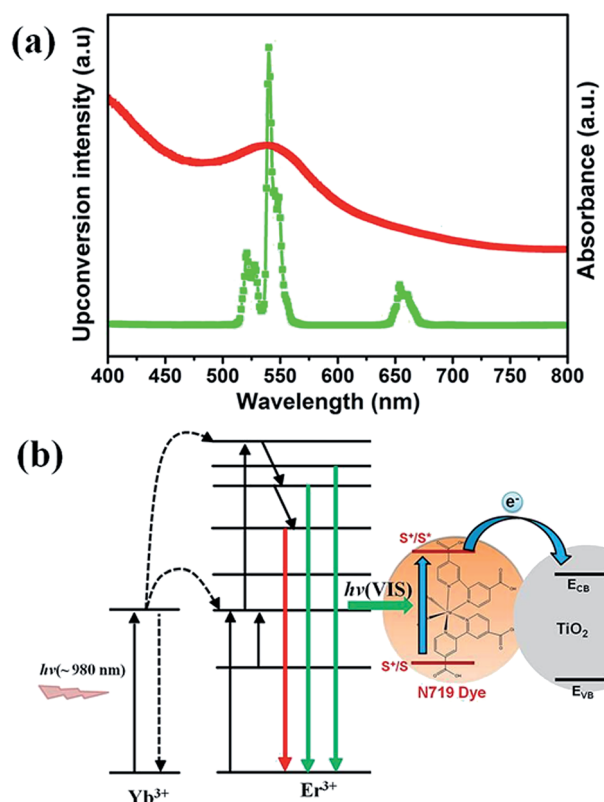**Fig. 14** (a) Absorption spectrum of N719 dye and UC photoluminescence spectrum of NaYF$_4$:Yb,Er nanoparticles. (b) Energy level diagram of upconversion DSSC shows the energy transfer from UC nanocrystals to the N719 dye.

consequence, the NIR light absorbed by the UCNPs can be effectively used to excite the dye molecules (Fig. 14b), which in turn will help increase the performance of DSSCs in the NIR region.

In 2010, Shan and Demopoulos reported for the first time the application of UCNPs for enhancing NIR sunlight harvesting in DSSCs.[205] In their studies, they prepared Yb^{3+} and Er^{3+}-*co*-doped LaF_3–TiO_2 nanocomposites and used them as an upconversion layer to fabricate a triple-layer working electrode for DSSCs. The green emission from the upconversion nanocomposite can be efficiently absorbed by the N719 dye, and generates the photo-current upon 980 nm laser excitation. However, this structure was ineffective and the overall efficiency of the DSSCs decreased due to apparent charge recombination at the UCNP/dye/electrolyte interfaces. Later, several research groups have successfully modified this strategy to improve the performance of DSSCs.[206–225] For example, Wu *et al.* reported enhanced photovoltaic performances of DSSCs by doping $Y_{0.78}Yb_{0.20}Er_{0.02}F_3$ in a TiO_2 photoanode. The DSSC with 7 wt% $Y_{0.78}Yb_{0.2}Er_{0.02}F_3/TiO_2$ in the doping layer exhibited higher short-circuit current density ($J_{SC} = 15.58$ mA cm^{-2}), open-circuit voltage ($V_{OC} = 0.80$ V), and a power conversion efficiency (η) of 7.90%, which is significantly higher than for the DSSC without a REF_3-doped TiO_2 layer ($J_{SC} = 13.33$ mA cm^{-2}, $V_{OC} = 0.73$ V, and $\eta = 5.84\%$). The enhanced J_{SC} mainly comes from the upcon-version luminescence of Yb^{3+}/Er^{3+}, which results in more inci-dent light harvesting. On the other hand, doping REF_3 in TiO_2 gives a p-type doping effect, which elevates the flat-band potential and the Fermi level of the TiO_2 electrode, thus increasing the V_{OC}.[206]

Chang *et al.* observed enhanced efficiency in DSSCs with *in situ*-prepared $TiO_2/NaYF_4$:Yb^{3+}, Er^{3+} nano-heterostructures on the TiO_2 photoanode of the DSSC.[207] The TiO_2 photoanodes were prepared by mixing different amounts of UCNPs with TiO_2 NPs and screen printing on the FTO glass, followed by heat treatment at 400 or 450 °C. In 450 °C-sintered samples some of the crystal phases between TiO_2 and the UCNPs disappeared and shared interfaces (nano-heterostructures) were formed, whereas in 400 °C-sintered samples UCNPs and TiO_2 had clear interfaces and no nano-heterostructures were formed (Fig. 15). They found that the formation of nano-heterostructures between TiO_2 and UCNPs facilitates effective electron injec-tion from the UCNPs to the conduction band (CB) of TiO_2, which is not possible in physically mixed samples. The DSSCs using the photoanodes containing the nano-heterostructure produced 17% higher efficiency than that of the device without UCNPs and 13% higher than that of the device con-taining physically mixed TiO_2 and UCNPs, which clearly high-lights the effect of the direct electron injection from UCNPs to the CB of TiO_2. Zhao and co-workers used a new scattering and upconverting layer composed of double-shell β-$NaYF_4$:Yb,Er/SiO_2/TiO_2 submicroplates on top of the transparent TiO_2 layer for DSSCs.[215,216] The β-$NaYF_4$:Yb,Er cores can harvest the NIR light and re-emit visible upconversion light, which broadens the absorption spectrum of the DSSC and more photoinduced electrons can be produced to enhance the photocurrent. The thin SiO_2 inner shell can act as an insulating layer to separate
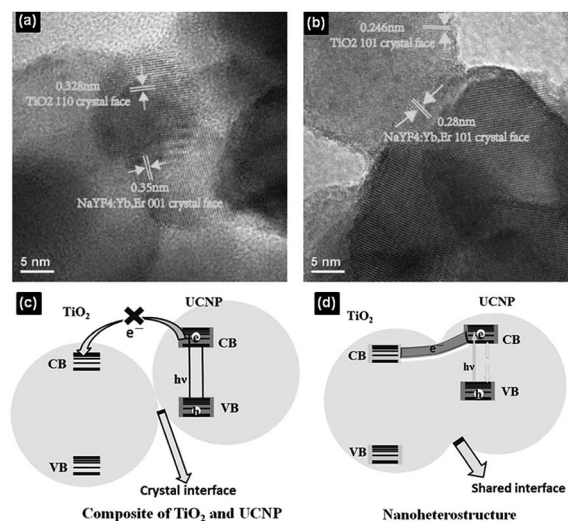

Fig. 15 HR-TEM images of TiO_2/UCNP nanocomposites sintered at (a) 400 °C and (b) 450 °C. Schematic representation of the (c) composite and (d) nanoheterostructure of TiO_2 and UCNPs. CB = conduction band. VB = valence band. Reprinted with permission from 201. Copyright 2013, WILEY-VCH Verlag GmbH & Co. KGaA, Weinheim.

the upconversion cores from the external environment and the recombination effect can be completely eliminated. The dye-loading ability was enhanced by the outer nanoporous TiO_2 shells. In addition, owing to the submicron dimensions, these microplates can act as effective Mie scatterers, leading to a significant enhancement of the light-harvesting capability. A DSSC employing a β-$NaYF_4$:Yb,Er/SiO_2/TiO_2 submicroplate top layer exhibited a 29.41% improvement in the energy conversion efficiency (7.70%) compared with a cell composed of nano-crystalline TiO_2 film (5.95%).[215] In a recent report, Wang and co-workers synthesized upconversion Yb^{3+}- and Er^{3+}-doped TiO_2 nanoshells and applied them to improve the performance of DSSCs. The upconverter-doped TiO_2 nanoshell acted as both the light scattering layer and the NIR-harvesting layer. An overall conversion efficiency of 9.12% was achieved with these dual-functional UC-TiO_2 hollow shells, corresponding to ~32.7% enhancement compared with the 6.87% efficiency for a P25 photoanode.[223]

Shan *et al.* proposed a new DSSC structure, in which the upconverting $NaYF_4$:Yb,Er microplates were placed on the rear side of the counter electrode.[212] This design enables a dual-mode functionality that provides both light reflection and NIR light harvesting. Under AM 1.5G filtered spectral illumination (100 mW cm^{-2}) approximately 10% enhancement in conversion efficiency was achieved. The observed enhancement was predominantly due to the light-reflecting action of the β-$NaYF_4$:Yb,Er. The upconversion contribution from the Er^{3+} and Yb^{3+} dopants was very low (~1%), and the authors concluded that more efficient UCNPs need to be developed to render upconversion a viable option in solar cell fabrication. Recently, our group developed a new strategy to improve the efficiency of DSSCs by using external NIR light-harvesting and light-reflecting bifunctional layers consisting of upconversion

nanoparticles combined with silver particles.[218] We used 30 mol% Fe^{3+}-doped β-NaGdF$_4$:Yb,Er UCNPs, which have 30 times more upconversion luminescence than the undoped UCNPs. The enhanced upconversion luminescence in Fe^{3+}-doped UCNPs can be more beneficial for solar cell applications. A schematic diagram of the DSSC structure is shown in Fig. 16. The rear reflector layer was fabricated on a microscopic glass slide by drop-casting 50 μL of silver particles, followed by drying at 70 °C. The upconversion nanoparticle layer was coated by dropping 50 μL of UCNPs (1 wt% in toluene) and dried at 80 °C for 2 min. Rear reflector films were attached to the counter electrode using Scotch tape or sealant (Surlyn, 60 μm thick, Meltonix). The UCNPs can harvest the NIR light and emit visible photons. Silver particles can function as a back reflector for the upconverted visible photons emitted from the UCNPs bouncing back into the DSSC. In addition, we found that silver particles further enhanced the upconversion luminescence by the plasmonic effect. A DSSC with a plasmonic and upconversion rear reflector achieved a conversion efficiency of 7.04% under one-sun illumination, which is an increase of 21.3% compared to a cell without a rear reflector (5.8%).[218]

Chen and co-workers demonstrated the potential application of UCNPs to construct implantable DSSCs to power next generation *in vivo* devices.[211] The authors prepared a 980 nm laser-driven photovoltaic cell (980LD-PVC) introducing a NaYF$_4$:Yb,Er nanophosphor layer into a conventional DSSC (Fig. 17). An ethanol dispersion of 1 mg mL^{-1} NaYF$_4$:Yb,Er nanorods was drop-casted on the N3 dye-sensitized TiO$_2$ film, followed by heating at 40 °C in air for 30 min to remove the ethanol. This casting process was repeated until a 4 μm thick NaYF$_4$:Yb,Er nanorod film was prepared. They further replaced the conventional liquid electrolyte with a highly thermostable succinonitrile-based gel electrolyte to avoid any leakage and evaporation of the solvent. Under the irradiation of a 980 nm laser with a power of 720 mW cm^{-2}, the 980LD-PVC produced an output power of 44.5 μW and an overall conversion efficiency of 0.039%. More importantly, after being covered with chicken skin (thickness: 1 mm) as a model of biological tissue, 980LD-
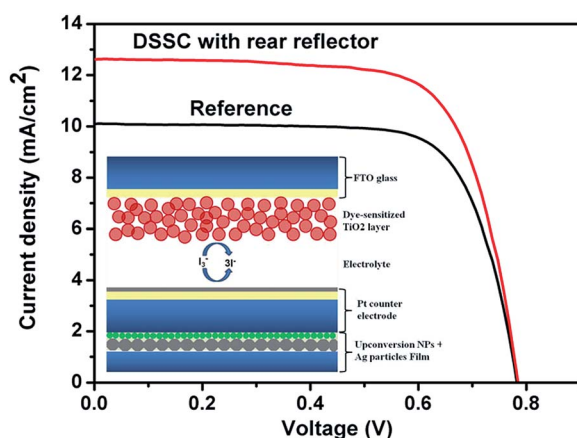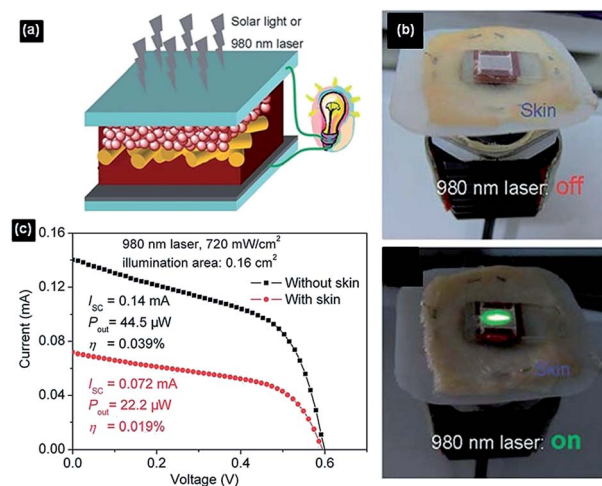

Fig. 17 (a) schematic illustration of 980LD-PVCs containing a NaYF$_4$:Yb,Er nanorod film. (b) Photos of TCO glass/N3-sensitized TiO$_2$ film/NaYF$_4$:Yb,Er film on the skin with the support, when a 980 nm laser turns off and on. (c) Photocurrent–voltage characteristics of 980LD-PVC without, and covered with, chicken skin, under irradiation of a 980 nm laser with an intensity of 720 mW cm^{-2}. Reproduced from Shan *et al.*[205] Copyright 2012, The Royal Society of Chemistry.

PVC still possesses a maximum output power of 22.2 μW and an overall conversion efficiency of 0.019%. This output power (22.2 μW) is excellent enough to satisfy the power requirements of many biological devices such as *in vivo* nanorobots (at least 1 μW) and cardiac pacemakers (about 10 μW). Although there are some biologically non-compatible components (such as the glass electrode) present in 980LD-PVCs, they can be potentially replaced by other biocompatible components such as a flexible plastic electrode.

5.4. Upconversion for organic solar cells

Organic solar cells are considered one of the promising candidates for low-cost photovoltaic cells because of their obvious advantages such as light weight, simple fabrication, flexibility and low cost. The best performing organic solar cells are made of bulk heterojunctions comprising of donor poly(3-hexylthiophene) (P3HT) and the acceptor fullerene derivative [6,6]-phenyl-C61-butyric acid methyl ester (PCBM). Upon excitation, the donor material absorbs the light and produces excitons, which are then transported to the donor/acceptor interface. From there, the electrons that exist in a higher energy state are transferred to the acceptor material and extracted at the cathode (metal electrode). Holes travel through the donor layer to the anode (transparent electrode). Most of the available donor materials work well only in the visible region, which ultimately affects the device efficiency. It is necessary to harvest the NIR photons to further improve the efficiency of organic solar cells.

In 2011, Wang and co-workers, demonstrated the feasibility of upconversion in P3HT:PCBM organic solar cells.[227] A commercial UC phosphor based on YF$_3$:Yb,Er with an UC quantum efficiency of 0.19% (excitation density: 250 mW cm^{-2})

Fig. 16 *J–V* curves of DSSCs with and without rear reflector films. Inset shows a schematic diagram of the DSSC with rear reflector film.

was used as UC source and they obtained a photocurrent density of *ca.* 16.5 µA cm^{-2} under a laser illumination intensity of *ca.* 25 mW cm^{-2}. Later in 2012, the same group reported the application of dual-functional upconverting Yb,Er-doped MoO$_3$ film in P3HT:PCBM solar cells.[228] The MoO$_3$ matrix acts as a hole extraction layer while the Yb^{3+}-sensitized Er^{3+} dopants upconvert the NIR photons. The authors found that the upconversion contribution to the short-circuit current was less than 1% under one-sun (AM 1.5G) illumination. Wu *et al.* applied NaYF$_4$:Yb,Er upconversion nanoparticles on the rear side of P3HT:PCBM solar cells and studied their effect on device performance under 980 nm laser illumination. The UC layer was fabricated by spray-coating a thick layer of UC nanoparticles from a hexane solution on the back side of the ITO glass substrate. They observed an enhancement of 5 µA in the short-circuit current and a maximum output power of 9.05 µW with a 980 nm laser. However, with illumination with simulated solar irradiation (AM 1.5G), the UC effects did not improve the device efficiency. The photocurrent of the device decreased significantly due to the scattering of incoming photons by the NaYF$_4$:Yb,Er film.[229]

Adikaari *et al.* demonstrated the application of Y$_2$BaZnO$_5$: Yb,Ho upconversion phosphors to PCDTBT:PCBM (PCDTBT: poly[*N*-9'-heptadecanyl-2,7-carbazole-alt-5,5-(4',7'-di-2-thienyl-2',1',3'-benzothiadiazole)]) organic solar cells in order to utilize the NIR solar spectrum.[230] The authors presented two different device configurations for the use of an UC phosphor with OPV devices. The UC phosphors were made as pellets using a press and placed as shown in Fig. 18. In the first configuration, the UC phosphor was placed in front of the device, while in the second configuration, the phosphor was placed on the rear side of the device. The PCDTBT:PCBM active layer mainly absorbs the visible photons, whereas Y$_2$BaZnO$_5$:Yb,Ho phosphors absorb in the NIR region of 870–1030 nm due to the $^2F_{7/2}$–$^2F_{5/2}$ (Yb^{3+}) transition. More importantly, the UC emission peak of the phosphor matches well with the absorption peak of the PCDTBT:PCBM active layer. They showed that when the upconversion phosphor is placed behind the device, a maximum photocurrent density of 16 µA cm^{-2} can be achieved when illuminated with a 986 nm laser (excitation density: ~390 mW cm^{-2}). Recently, Guo and co-workers, doped NaYF$_4$:Yb,Er nanocomposites into a PCDTBT:PCBM blend as a bifunctional

additive to improve the performance of inverted polymer BHJ solar cells. The doped UC nanocomposites exhibited both the NIR light-harvesting as well as light-scattering properties, which enhanced the device performance. With optimized device fabrication, a PCE of 6.87% was obtained, which is 19.1% higher than that of the device without upconversion nanocomposites.[231]

6. Conclusions and perspectives

In this review, we have presented the advances in the synthesis and solar cell applications of upconversion nanomaterials. One of the major challenges affecting solar cell efficiencies is the spectral mismatch between the incident solar spectrum and the semiconductor. Most of the sub-band-gap photons are not absorbed by the semiconductor and are transmitted. This decreases the cell efficiency to a large extent. Spectral converters, such as upconversion nanomaterials, which can convert NIR light into visible light, have shown promising applications to reduce the transparency losses in large bandgap semiconductor solar cells. However, there are major drawbacks associated with upconversion materials, limiting the practical application of upconverters for solar cells. First, the efficiency of upconversion nanomaterials used for solar cells is very low and needs to be improved. Different methods available to improve the UC efficiency, such as impurity doping, use of plasmonic structures and construction of core–shell UC nanomaterials, have been discussed in this review. The impurity doping strategy has exhibited great potential as a simple and efficient method to improve UC emissions. Secondly, only a very small fraction of sub-band-gap sunlight can be upconverted due to the narrow absorption cross-section of Ln^{3+} ions. Broadening the absorption spectrum is another area that needs more attention. There are only a few studies that have been performed in this area. Broadening the absorption spectrum for lanthanide upconverters can be achieved by employing external sensitizers such as quantum dots[232] or organic dyes.[233] These sensitizers can absorb over a broad range and emit in the lanthanide absorption region. Pan *et al.* proved the viability of this method in c-Si solar cells by placing PbS QDs below the upconverter layer. They have experimentally proved that the combination of Yb, Er-doped phosphor with QDs enhances the upconversion and the increased upconverted emissions resulted in higher currents in the solar cell. Another approach to broaden the absorption spectrum is to use Nd^{3+} as a second sensitizer to sensitize the first sensitizer Yb^{3+}.[234,235] Nd^{3+} has multiple NIR excitation bands at wavelengths shorter than 980 nm, such as 730, 808, and 865 nm, which favours broadband absorption. With a large absorption cross-section, Nd^{3+} can absorb shorter wavelength light effectively and transfer its energy to Yb^{3+}. Investigation of these issues is still in the initial stage and the application to solar cells is comparatively small. Despite the significant progress, there are many exciting areas available for
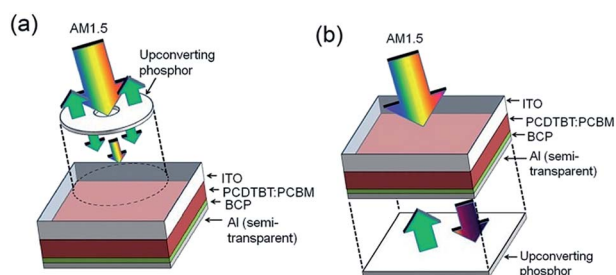

Fig. 18 Schematic of the organic photovoltaic device with an upconversion phosphor placed (a) in front of and (b) behind the device. Reprinted with permission from ref. 230. Copyright 2012, American Institute of Physics.

researchers to explore the practical application of upconversion nanomaterials as spectral converters for solar cells.

Acknowledgements

Notes and references

1 A. J. Nozik and J. Miller, *Chem. Rev.*, 2010, **110**, 6443–6445.
2 K. Kalyanasundaram and M. Gratzel, *J. Mater. Chem.*, 2012, **22**, 24190–24194.
3 H. Aguas, S. K. Ram, A. Araujo, D. Gaspar, A. Vicente, S. A. Filonovich, E. Fortunato, R. Martins and I. Ferreira, *Energy Environ. Sci.*, 2011, **4**, 4620–4632.
4 G. Conibeer, *Mater. Today*, 2007, **10**, 42–50.
5 D. M. Powell, M. T. Winkler, H. J. Choi, C. B. Simmons, D. B. Needleman and T. Buonassisi, *Energy Environ. Sci.*, 2012, **5**, 5874–5883.
6 R. D. Costa, F. Lodermeyer, R. Casillas and D. M. Guldi, *Energy Environ. Sci.*, 2014, **7**, 1281–1296.
7 W. Shockley and H. J. Queisser, *J. Appl. Phys.*, 1961, **32**, 510–519.
8 B. O'Regan and M. Gratzel, *Nature*, 1991, **353**, 737–740.
9 M. Law, L. E. Greene, J. C. Johnson, R. Saykally and P. D. Yang, *Nat. Mater.*, 2005, **4**, 455–459.
10 E. H. Sargent, *Nat. Photonics*, 2012, **6**, 133–135.
11 G. Li, V. Shrotriya, J. S. Huang, Y. Yao, T. Moriarty, K. Emery and Y. Yang, *Nat. Mater.*, 2005, **4**, 864–868.
12 P.-L. T. Boudreault, A. Najari and M. Leclerc, *Chem. Mater.*, 2010, **23**, 456–469.
13 T. Todorov and D. B. Mitzi, *Eur. J. Inorg. Chem.*, 2010, 17–28.
14 B. S. Richards, *Sol. Energy Mater. Sol. Cells*, 2006, **90**, 2329–2337.
15 M. S. Leite, R. L. Woo, J. N. Munday, W. D. Hong, S. Mesropian, D. C. Law and H. A. Atwater, *Appl. Phys. Lett.*, 2013, **102**, 033901.
16 K. X. Wang, Z. Yu, V. Liu, Y. Cui and S. Fan, *Nano Lett.*, 2012, **12**, 1616–1619.
17 J. Grandidier, D. M. Callahan, J. N. Munday and H. A. Atwater, *Adv. Mater.*, 2011, **23**, 1272–1276.
18 R. J. Veenkamp and W. N Ye, *J. Appl. Phys.*, 2014, **115**, 124317.
19 Q. Y. Zhang and X. Y. Huang, *Prog. Mater. Sci.*, 2010, **55**, 353–427.
20 T. Trupke, M. A. Green and P. Wurfel, *J. Appl. Phys.*, 2002, **92**, 4117–4122.
21 F. Auzel, *Chem. Rev.*, 2003, **104**, 139–174.
22 G. Blasse and B. C. Grabmaier, *Luminescent Materials*, Springer, Berlin, 1994.
23 T. N. Singh-Rachford and F. N. Castellano, *Coord. Chem. Rev.*, 2010, **254**, 2560–2573.
24 J. S. Chivian, W. E. Case and D. D. Eden, *Appl. Phys. Lett.*, 1979, **35**, 124.
25 G. H. Dieke, *Spectra and Energy Levels of Rare Earth Ions in Crystals*, Wiley, New York, 1968.
26 F. Wang and X. Liu, *Chem. Soc. Rev.*, 2009, **38**, 976–989.
27 J. Ohwaki and Y. Wang, *Jpn. J. Appl. Phys.*, 1994, **33**, L334–L337.
28 F. Auzel, D. Pecile and D. Morin, *J. Electrochem. Soc.*, 1975, **122**, 101–107.
29 P. P. Fedorov, A. A. Luginina, S. V. Kuznetsov and V. V. Osiko, *J. Fluorine Chem.*, 2011, **132**, 1012–1039.
30 F. Vetrone and J. A. Capobianco, *Int. J. Nanotechnol.*, 2008, **5**, 1306–1339.
31 Y.-W. Zhang, X. Sun, R. Si, L.-P. You and C.-H. Yan, *J. Am. Chem. Soc.*, 2005, **127**, 3260–3261.
32 J.-C. Boyer, F. Vetrone, L. A. Cuccia and J. A. Capobianco, *J. Am. Chem. Soc.*, 2006, **128**, 7444–7445.
33 J.-C. Boyer, L. A. Cuccia and J. A. Capobianco, *Nano Lett.*, 2007, **7**, 847–852.
34 H.-X. Mai, Y.-W. Zhang, L.-D. Sun and C.-H. Yan, *J. Phys. Chem. C*, 2007, **111**, 13730–13739.
35 H.-X. Mai, Y.-W. Zhang, R. Si, Z.-G. Yan, L.-d. Sun, L.-P. You and C.-H. Yan, *J. Am. Chem. Soc.*, 2006, **128**, 6426–6436.
36 Y.-P. Du, Y.-W. Zhang, L.-D. Sun and C.-H. Yan, *Dalton Trans.*, 2009, 8574–8581.
37 X. Ye, J. E. Collins, Y. Kang, J. Chen, D. T. N. Chen, A. G. Yodh and C. B. Murray, *Proc. Natl. Acad. Sci. U. S. A.*, 2010, **107**, 22430–22435.
38 G. S. Yi and G. M. Chow, *Adv. Funct. Mater.*, 2006, **16**, 2324–2329.
39 J. Shan, X. Qin, N. Yao and Y. Ju, *Nanotechnology*, 2007, **18**, 445607.
40 W. Kong, R. Wei, N. Yao and Y. Ju, *J. Appl. Phys.*, 2010, **107**, 054901.
41 J. Shan and Y. Ju, *Appl. Phys. Lett.*, 2007, **91**, 123103.
42 Y. Wei, F. Lu, X. Zhang and D. Chen, *Chem. Mater.*, 2006, **18**, 5733–5737.
43 C. Liu, H. Wang, X. Zhang and D. Chen, *J. Mater. Chem.*, 2009, **19**, 489–496.
44 C. Liu, H. Wang, X. Li and D. Chen, *J. Mater. Chem.*, 2009, **19**, 3546–3553.
45 H. Na, K. Woo, K. Lim and H. S. Jang, *Nanoscale*, 2013, **5**, 4242–4251.
46 X. Li, S. Gai, C. Li, D. Wang, N. Niu, F. He and P. Yang, *Inorg. Chem.*, 2012, **51**, 3963–3971.
47 G. K. Das and T. T. Y. Tan, *J. Phys. Chem. C*, 2008, **112**, 11211–11217.
48 G. K. Das, B. C. Heng, S.-C. Ng, T. White, J. S. C. Loo, L. D'Silva, P. Padmanabhan, K. K. Bhakoo, S. T. Selvan and T. T. Y. Tan, *Langmuir*, 2010, **26**, 8959–8965.
49 T. Paik, T. R. Gordon, A. M. Prantner, H. Yun and C. B. Murray, *ACS Nano*, 2013, **7**, 2850–2859.
50 R. Si, Y.-W. Zhang, H.-P. Zhou, L.-D. Sun and C.-H. Yan, *Chem. Mater.*, 2006, **19**, 18–27.
51 R. Si, Y.-W. Zhang, L.-P. You and C.-H. Yan, *Angew. Chem., Int. Ed.*, 2005, **44**, 3256–3260.
52 Z. Li and Y. Zhang, *Nanotechnology*, 2008, **19**, 345606.
53 F. Shi, J. Wang, D. Zhang, G. Qin and W. Qin, *J. Mater. Chem.*, 2011, **21**, 13413–13421.

54 C. Zhao, X. Kong, X. Liu, L. Tu, F. Wu, Y. Zhang, K. Liu, Q. Zeng and H. Zhang, *Nanoscale*, 2013, **5**, 8084–8089.

55 J. Zhao, Z. Lu, Y. Yin, C. McRae, J. A. Piper, J. M. Dawes, D. Jin and E. M. Goldys, *Nanoscale*, 2013, **5**, 944–952.

56 W. Niu, L. T. Su, R. Chen, H. Chen, Y. Wang, A. Palaniappan, H. Sun and A. I. Yoong Tok, *Nanoscale*, 2014, **6**, 817–824.

57 P. Ramasamy, P. Chandra, S. W. Rhee and J. Kim, *Nanoscale*, 2013, **5**, 8711–8717.

58 F. Shi, J. Wang, X. Zhai, D. Zhao and W. Qin, *CrystEngComm*, 2011, **13**, 3782–3787.

59 G. K. Das, N. J. J. Johnson, J. Cramen, B. Blasiak, P. Latta, B. Tomanek and F. C. J. M. van Veggel, *J. Phys. Chem. Lett.*, 2012, **3**, 524–529.

60 G. Chen, T. Y. Ohulchanskyy, W. C. Law, H. Agren and P. N. Prasad, *Nanoscale*, 2011, **3**, 2003–2008.

61 C. T. Xu, P. Svenmarker, H. Liu, X. Wu, M. E. Messing, L. R. Wallenberg and S. Andersson-Engels, *ACS Nano*, 2012, **6**, 4788–4795.

62 Q. Zeng, B. Xue, Y. Zhang, D. Wang, X. Liu, L. Tu, H. Zhao, X. Kong and H. Zhang, *CrystEngComm*, 2013, **15**, 4765–4772.

63 R. Deng, X. Xie, M. Vendrell, Y.-T. Chang and X. Liu, *J. Am. Chem. Soc.*, 2011, **133**, 20168–20171.

64 G. Jiang, J. Pichaandi, N. J. J. Johnson, R. D. Burke and F. C. J. M. van Veggel, *Langmuir*, 2012, **28**, 3239–3247.

65 W. Ren, G. Tian, S. Jian, Z. Gu, L. Zhou, L. Yan, S. Jin, W. Yin and Y. Zhao, *RSC Adv.*, 2012, **2**, 7037–7041.

66 F. Wang, J. Wang and X. Liu, *Angew. Chem., Int. Ed.*, 2010, **49**, 7456–7460.

67 H. Schäfer, P. Ptacek, O. Zerzouf and M. Haase, *Adv. Funct. Mater.*, 2008, **18**, 2913–2918.

68 H.-T. Wong, F. Vetrone, R. Naccache, H. L. W. Chan, J. Hao and J. A. Capobianco, *J. Mater. Chem.*, 2011, **21**, 16589–16596.

69 F. Zhang, R. Che, X. Li, C. Yao, J. Yang, D. Shen, P. Hu, W. Li and D. Zhao, *Nano Lett.*, 2012, **12**, 2852–2858.

70 Y. I. Park, H. M. Kim, J. H. Kim, K. C. Moon, B. Yoo, K. T. Lee, N. Lee, Y. Choi, W. Park, D. Ling, K. Na, W. K. Moon, S. H. Choi, H. S. Park, S.-Y. Yoon, Y. D. Suh, S. H. Lee and T. Hyeon, *Adv. Mater.*, 2012, **24**, 5755–5761.

71 F. Chen, W. Bu, S. Zhang, J. Liu, W. Fan, L. Zhou, W. Peng and J. Shi, *Adv. Funct. Mater.*, 2013, **23**, 298–307.

72 H.-S. Qian and Y. Zhang, *Langmuir*, 2008, **24**, 12123–12125.

73 J. Pichaandi, J.-C. Boyer, K. R. Delaney and F. C. J. M. van Veggel, *J. Phys. Chem. C*, 2011, **115**, 19054–19064.

74 M. Banski, A. Podhorodecki and J. Misiewicz, *Phys. Chem. Chem. Phys.*, 2013, **15**, 19232–19241.

75 A. A. Arnold, V. Terskikh, Q. Y. Li, R. Naccache, I. Marcotte and J. A. Capobianco, *J. Phys. Chem. C*, 2013, **117**, 25733–25741.

76 Y. Deng, H. Wang, W. Gu, S. Li, N. Xiao, C. Shao, Q. Xu and L. Ye, *J. Mater. Chem. B*, 2014, **2**, 1521–1529.

77 N. J. J. Johnson, W. Oakden, G. J. Stanisz, R. Scott Prosser and F. C. J. M. van Veggel, *Chem. Mater.*, 2011, **23**, 3714–3722.

78 H. Xing, S. Zhang, W. Bu, X. Zheng, L. Wang, Q. Xiao, D. Ni, J. Zhang, L. Zhou, W. Peng, K. Zhao, Y. Hua and J. Shi, *Adv. Mater.*, 2014, **26**, 3867–3872.

79 G. Chen, J. Shen, T. Y. Ohulchanskyy, N. J. Patel, A. Kutikov, Z. Li, J. Song, R. K. Pandey, H. Ågren, P. N. Prasad and G. Han, *ACS Nano*, 2012, **6**, 8280–8287.

80 X. Teng, Y. Zhu, W. Wei, S. Wang, J. Huang, R. Naccache, W. Hu, A. I. Y. Tok, Y. Han, Q. Zhang, Q. Fan, W. Huang, J. A. Capobianco and L. Huang, *J. Am. Chem. Soc.*, 2012, **134**, 8340–8343.

81 M. Pang, J. Feng, S. Song, Z. Wang and H. Zhang, *CrystEngComm*, 2013, **15**, 6901–6904.

82 X. Sun, Y.-W. Zhang, Y.-P. Du, Z.-G. Yan, R. Si, L.-P. You and C.-H. Yan, *Chem.–Eur. J.*, 2007, **13**, 2320–2332.

83 H. Qiu, G. Chen, R. Fan, L. Yang, C. Liu, S. Hao, M. J. Sailor, H. gren, C. Yang and P. N. Prasad, *Nanoscale*, 2014, **6**, 753–757.

84 Y.-P. Du, X. Sun, Y.-W. Zhang, Z.-G. Yan, L.-D. Sun and C.-H. Yan, *Cryst. Growth Des.*, 2009, **9**, 2013–2019.

85 D. Chen, Y. Yu, F. Huang, H. Lin, P. Huang, A. Yang, Z. Wang and Y. Wang, *J. Mater. Chem.*, 2012, **22**, 2632–2640.

86 D. Chen, Y. Yu, F. Huang, P. Huang, A. Yang, Z. Wang and Y. Wang, *Chem. Commun.*, 2011, **47**, 11083–11085.

87 J. Wang, F. Wang, C. Wang, Z. Liu and X. Liu, *Angew. Chem., Int. Ed.*, 2011, **50**, 10369–10372.

88 Y. Zhang, J. D. Lin, V. Vijayaragavan, K. K. Bhakoo and T. T. Y. Tan, *Chem. Commun.*, 2012, **48**, 10322–10324.

89 G. Yi, Y. Peng and Z. Gao, *Chem. Mater.*, 2011, **23**, 2729–2734.

90 X. Wang and Y. Li, *Chem.–Eur. J.*, 2003, **9**, 5627–5635.

91 X. Wang and Y. Li, *Angew. Chem., Int. Ed.*, 2002, **41**, 4790–4793.

92 X. Wang, X. M. Sun, D. Yu, B. S. Zou and Y. Li, *Adv. Mater.*, 2003, **15**, 1442–1445.

93 F. Zhang and D. Zhao, *ACS Nano*, 2008, **3**, 159–164.

94 Z. Xu, C. Li, P. Yang, C. Zhang, S. Huang and J. Lin, *Cryst. Growth Des.*, 2009, **9**, 4752–4758.

95 X. Wang, J. Zhuang, Q. Peng and Y. Li, *Nature*, 2005, **437**, 121–124.

96 L. Wang and Y. Li, *Nano Lett.*, 2006, **6**, 1645–1649.

97 X. Wang, J. Zhuang, Q. Peng and Y. Li, *Inorg. Chem.*, 2006, **45**, 6661–6665.

98 L. Wang and Y. Li, *Chem. Mater.*, 2007, **19**, 727–734.

99 F. Zhang, Y. Wan, T. Yu, F. Zhang, Y. Shi, S. Xie, Y. Li, L. Xu, B. Tu and D. Zhao, *Angew. Chem., Int. Ed.*, 2007, **119**, 8122–8125.

100 P. Li, Q. Peng and Y. Li, *Adv. Mater.*, 2009, **21**, 1945–1948.

101 G. Wang, Q. Peng and Y. Li, *J. Am. Chem. Soc.*, 2009, **131**, 14200–14201.

102 F. Wang, Y. Han, C. S. Lim, Y. H. Lu, J. Wang, J. Xu, H. Chen, C. Zhang, M. Hong and X. Liu, *Nature*, 2010, **463**, 1061–1065.

103 D. Chen, Y. Yu, F. Huang, P. Huang, A. Yang and Y. Wang, *J. Am. Chem. Soc.*, 2010, **132**, 9976–9978.

104 D. Yang, Y. Dai, P. Ma, X. Kang, Z. Cheng, C. Li and J. Lin, *Chem.–Eur. J.*, 2013, **19**, 2685–2694.

105 G. Tian, Z. Gu, L. Zhou, W. Yin, X. Liu, L. Yan, S. Jin, W. Ren, G. Xing, S. Li and Y. Zhao, *Adv. Mater.*, 2012, **24**, 1226–1231.

106 G. Wang, Q. Peng and Y. Li, *Chem. Commun.*, 2010, **46**, 7528–7529.

107 Z.-j. Liu, X.-x. Song and Q. Tang, *Nanoscale*, 2013, **5**, 5073–5079.

108 Z. Bai, H. Lin, J. Johnson, S. C. Rong Gui, K. Imakita, R. Montazami, M. Fujii and N. Hashemi, *J. Mater. Chem. C*, 2014, **2**, 1736–1741.

109 C. Li, Z. Quan, J. Yang, P. Yang and J. Lin, *Inorg. Chem.*, 2007, **46**, 6329–6337.

110 C. Li, J. Yang, P. Yang, X. Zhang, H. Lian and J. Lin, *Cryst. Growth Des.*, 2008, **8**, 923–929.

111 C. Li, Z. Quan, P. Yang, J. Yang, H. Lian and J. Lin, *J. Mater. Chem.*, 2008, **18**, 1353–1361.

112 F. He, P. Yang, D. Wang, N. Niu, S. Gai and X. Li, *Inorg. Chem.*, 2011, **50**, 4116–4124.

113 J. H. Zeng, J. Su, Z. H. Li, R. X. Yan and Y. D. Li, *Adv. Mater.*, 2005, **17**, 2119–2123.

114 H. Qiu, G. Chen, L. Sun, S. Hao, G. Han and C. Yang, *J. Mater. Chem.*, 2011, **21**, 17202–17208.

115 H. Chen, X. Zhai, D. Li, L. Wang, D. Zhao and W. Qin, *J. Alloys Compd.*, 2012, **511**, 70–73.

116 P. Qiu, N. Zhou, Y. Wang, C. Zhang, Q. Wang, R. Sun, G. Gao and D. Cui, *CrystEngComm*, 2014, **16**, 1859–1863.

117 F. Wang, D. K. Chatterjee, Z. Li, Y. Zhang, X. Fan and M. Wang, *Nanotechnology*, 2006, **17**, 5786–5791.

118 F. Wang and X. Liu, *J. Am. Chem. Soc.*, 2008, **130**, 5642–5643.

119 F. Vetrone, R. Naccache, A. Juarranz de la Fuente, F. Sanz-Rodriguez, A. Blazquez-Castro, E. M. Rodriguez, D. Jaque, J. G. Sole and J. A. Capobianco, *Nanoscale*, 2010, **2**, 495–498.

120 G. Tian, L. Duan, X. Zhang, W. Yin, L. Yan, L. Zhou, X. Liu, X. Zheng, J. Li, Z. Gu and Y. Zhao, *Chem.–Asian J.*, 2014, **9**, 1655–1662.

121 Z. Wang, C. Liu, L. Chang and Z. Li, *J. Mater. Chem.*, 2012, **22**, 12186–12192.

122 F. Zhang, J. Li, J. Shan, L. Xu and D. Zhao, *Chem.–Eur. J.*, 2009, **15**, 11010–11019.

123 H.-T. Wong, M.-K. Tsang, C.-F. Chan, K.-L. Wong, B. Fei and J. Hao, *Nanoscale*, 2013, **5**, 3465–3473.

124 S. Wu, N. Duan, X. Ma, Y. Xia, H. Wang, Z. Wang and Q. Zhang, *Anal. Chem.*, 2012, **84**, 6263–6270.

125 H. Liu, W. Lu, H. Wang, L. Rao, Z. Yi, S. Zeng and J. Hao, *Nanoscale*, 2013, **5**, 6023–6029.

126 Q. Zhao, B. Shao, W. Lü, Y. Jia, W. Lv, M. Jiao and H. You, *Cryst. Growth Des.*, 2014, **14**, 1819–1826.

127 B.-L. An, L.-H. Ma, J.-H. Fang, Y.-Q. Wang and J.-Q. Xu, *RSC Adv.*, 2013, **3**, 19909–19912.

128 L. Guo, Y. Wang, Z. Zou, B. Wang, X. Guo, L. Han and W. Zeng, *J. Mater. Chem. C*, 2014, **2**, 2765–2772.

129 S. Gong, Z. Ren, S. Jiang, M. Li, X. Li, X. Wei, G. Xu, G. Shen and G. Han, *J. Phys. Chem. C*, 2014, **118**, 5486–5493.

130 W. Yin, L. Zhao, L. Zhou, Z. Gu, X. Liu, G. Tian, S. Jin, L. Yan, W. Ren, G. Xing and Y. Zhao, *Chem. Eur. J*, 2012, **18**, 9239–9245.

131 W. Yin, L. Zhou, Z. Gu, G. Tian, S. Jin, L. Yan, X. Liu, G. Xing, W. Ren, F. Liu, Z. Pan and Y. Zhao, *J. Mater. Chem.*, 2012, **22**, 6974–6981.

132 L. Zhou, Z. Gu, X. Liu, W. Yin, G. Tian, L. Yan, S. Jin, W. Ren, G. Xing, W. Li, X. Chang, Z. Hu and Y. Zhao, *J. Mater. Chem.*, 2012, **22**, 966–974.

133 G. Li, M. Shang, D. Geng, D. Yang, C. Peng, Z. Cheng and J. Lin, *CrystEngComm*, 2012, **14**, 2100–2111.

134 Y. Song, Y. Huang, L. Zhang, Y. Zheng, N. Guo and H. You, *RSC Adv.*, 2012, **2**, 4777–4781.

135 J. W. Stouwdam and F. C. J. M. van Veggel, *Nano Lett.*, 2002, **2**, 733–737.

136 G. Yi, H. Lu, S. Zhao, Y. Ge, W. Yang, D. Chen and L.-H. Guo, *Nano Lett.*, 2004, **4**, 2191–2196.

137 F. He, N. Niu, L. Wang, J. Xu, Y. Wang, G. Yang, S. Gai and P. Yang, *Dalton Trans.*, 2013, **42**, 10019–10028.

138 G.-S. Yi and G.-M. Chow, *J. Mater. Chem.*, 2005, **15**, 4460–4464.

139 K. Zheng, W. Song, C. Lv, Z. Liu and W. Qin, *CrystEngComm*, 2014, **16**, 4329–4337.

140 Q. Lu, Y. Hou, A. Tang, Y. Lu, L. Lv and F. Teng, *J. Appl. Phys.*, 2014, **115**, 074309–074304.

141 H. J. Kitchen, S. R. Vallance, J. L. Kennedy, N. Tapia-Ruiz, L. Carassiti, A. Harrison, A. G. Whittaker, T. D. Drysdale, S. W. Kingman and D. H. Gregory, *Chem. Rev.*, 2013, **114**, 1170–1206.

142 H.-Q. Wang and T. Nann, *ACS Nano*, 2009, **3**, 3804–3808.

143 C. Mi, Z. Tian, C. Cao, Z. Wang, C. Mao and S. Xu, *Langmuir*, 2011, **27**, 14632–14637.

144 N. Niu, F. He, S. Gai, C. Li, X. Zhang, S. Huang and P. Yang, *J. Mater. Chem.*, 2012, **22**, 21613–21623.

145 F. Li, C. Li, X. Liu, Y. Chen, T. Bai, L. Wang, Z. Shi and S. Feng, *Chem.–Eur. J.*, 2012, **18**, 11641–11646.

146 S. Pan, R. Deng, J. Feng, S. Song, S. Wang, M. Zhu and H. Zhang, *CrystEngComm*, 2013, **15**, 7640–7643.

147 E. R. Parnham and R. E. Morris, *Acc. Chem. Res.*, 2007, **40**, 1005–1013.

148 V. I. Pârvulescu and C. Hardacre, *Chem. Rev.*, 2007, **107**, 2615–2665.

149 X. Liu, J. Zhao, Y. Sun, K. Song, Y. Yu, C. Du, X. Kong and H. Zhang, *Chem. Commun.*, 2009, 6628–6630.

150 C. Chen, L.-D. Sun, Z.-X. Li, L.-L. Li, J. Zhang, Y.-W. Zhang and C.-H. Yan, *Langmuir*, 2010, **26**, 8797–8803.

151 G. Glaspell, J. Anderson, J. R. Wilkins and M. S. El-Shall, *J. Phys. Chem. C*, 2008, **112**, 11527–11531.

152 X. Qin, T. Yokomori and Y. Ju, *Appl. Phys. Lett.*, 2007, **90**, 073104.

153 W. Kong, J. Shan and Y. Ju, *Mater. Lett.*, 2010, **64**, 688–691.

154 F. Wang, R. Deng and X. Liu, *Nat. Protoc.*, 2014, **9**, 1634–1644.

155 R. H. Page, K. I. Schaffers, P. A. Waide, J. B. Tassano, S. A. Payne, W. F. Krupke and W. K. Bischel, *J. Opt. Soc. Am. B*, 1998, **15**, 996–1008.

156 J.-C. Boyer and F. C. J. M. van Veggel, *Nanoscale*, 2010, **2**, 1417–1419.

157 D. Chen and Y. Wang, *Nanoscale*, 2013, **5**, 4621–4637.

158 G. Y. Chen, H. C. Liu, G. Somesfalean, Y. Q. Sheng, H. J. Liang, Z. G. Zhang, Q. Sun and F. P. Wang, *Appl. Phys. Lett.*, 2008, **92**, 113114.

159 G. Chen, H. Liu, H. Liang, G. Somesfalean and Z. Zhang, *J. Phys. Chem. C*, 2008, **112**, 12030–12036.

160 V. Mahalingam, R. Naccache, F. Vetrone and J. A. Capobianco, *Opt. Express*, 2012, **20**, 111–119.

161 Q. Cheng, J. Sui and W. Cai, *Nanoscale*, 2012, **4**, 779–784.

162 D. Yang, Y. Dai, P. a. Ma, X. Kang, M. Shang, Z. Cheng, C. Li and J. Lin, *J. Mater. Chem.*, 2012, **22**, 20618–20625.

163 Q. Dou and Y. Zhang, *Langmuir*, 2011, **27**, 13236–13241.

164 Q. Huang, J. Yu, E. Ma and K. Lin, *J. Phys. Chem. C*, 2010, **114**, 4719–4724.

165 L. Lei, D. Chen, P. Huang, J. Xu, R. Zhang and Y. Wang, *Nanoscale*, 2013, **5**, 11298–11305.

166 H. Zhang, D. Xu, Y. Huang and X. Duan, *Chem. Commun.*, 2011, **47**, 979–981.

167 W. Xu, S. Xu, Y. Zhu, T. Liu, X. Bai, B. Dong, L. Xu and H. Song, *Nanoscale*, 2012, **4**, 6971–6973.

168 M. Saboktakin, X. Ye, S. J. Oh, S.-H. Hong, A. T. Fafarman, U. K. Chettiar, N. Engheta, C. B. Murray and C. R. Kagan, *ACS Nano*, 2012, **6**, 8758–8766.

169 W. Zhang, F. Ding and S. Y. Chou, *Adv. Mater.*, 2012, **24**, OP236–OP241.

170 M. Saboktakin, X. Ye, U. K. Chettiar, N. Engheta, C. B. Murray and C. R. Kagan, *ACS Nano*, 2013, **7**, 7186–7192.

171 Q.-C. Sun, H. Mundoor, J. C. Ribot, V. Singh, I. I. Smalyukh and P. Nagpal, *Nano Lett.*, 2013, **14**, 101–106.

172 H. Zhang, Y. Li, I. A. Ivanov, Y. Qu, Y. Huang and X. Duan, *Angew. Chem., Int. Ed.*, 2010, **49**, 2865–2868.

173 Z. Q. Li, S. Chen, J. J. Li, Q. Q. Liu, Z. Sun, Z. B. Wang and S. M. Huang, *J. Appl. Phys.*, 2012, **111**, 014310.

174 P. Yuan, Y. H. Lee, M. K. Gnanasammandhan, Z. Guan, Y. Zhang and Q.-H. Xu, *Nanoscale*, 2012, **4**, 5132–5137.

175 Z. Li, L. Wang, Z. Wang, X. Liu and Y. Xiong, *J. Phys. Chem. C*, 2011, **115**, 3291–3296.

176 F. Zhang, G. B. Braun, Y. Shi, Y. Zhang, X. Sun, N. O. Reich, D. Zhao and G. Stucky, *J. Am. Chem. Soc.*, 2010, **132**, 2850–2851.

177 G.-S. Yi and G.-M. Chow, *Chem. Mater.*, 2006, **19**, 341–343.

178 Y.-F. Wang, L.-D. Sun, J.-W. Xiao, W. Feng, J.-C. Zhou, J. Shen and C.-H. Yan, *Chem.–Eur. J.*, 2012, **18**, 5558–5564.

179 F. Vetrone, R. Naccache, V. Mahalingam, C. G. Morgan and J. A. Capobianco, *Adv. Funct. Mater.*, 2009, **19**, 2924–2929.

180 F. Wang, R. Deng, J. Wang, Q. Wang, Y. Han, H. Zhu, X. Chen and X. Liu, *Nat. Mater.*, 2011, **10**, 968–973.

181 P. Gibart, F. Auzel, J. C. Guillaume and K. Zahraman, *Jpn. J. Appl. Phys., Part 1*, 1996, **35**, 4401–4402.

182 A. Shalav, B. S. Richards, T. Trupke, K. W. Krämer and H. U. Güdel, *Appl. Phys. Lett.*, 2005, **86**, 013505.

183 S. Fischer, J. C. Goldschmidt, P. Löper, G. H. Bauer, R. Brüggemann, K. Krämer, D. Biner, M. Hermle and S. W. Glunz, *J. Appl. Phys.*, 2010, **108**, 044912.

184 S. Ivanova, F. Pelle, A. Tkachuk, M. F. Joubert, Y. Guyot and V. P. Gapontsev, *J. Lumin.*, 2008, **128**, 914–917.

185 X. F. Liang, X. Y. Huang and Q. Y. Zhang, *J. Fluoresc.*, 2009, **19**, 285–289.

186 F. Xin, S. Zhao, L. Huang, D. Deng, G. Jia, H. Wang and S. Xu, *Mater. Lett.*, 2012, **78**, 75–77.

187 X. F. Wang, X. H. Yan and C. X. Kan, *J. Mater. Chem.*, 2011, **21**, 4251–4256.

188 R. Martín-Rodríguez, S. Fischer, A. Ivaturi, B. Froehlich, K. W. Krämer, J. C. Goldschmidt, B. S. Richards and A. Meijerink, *Chem. Mater.*, 2013, **25**, 1912–1921.

189 S. Ivanova and F. Pelle, *J. Opt. Soc. Am. B*, 2009, **26**, 1930–1938.

190 A. Boccolini, R. Faoro, E. Favilla, S. Veronesi and M. Tonelli, *J. Appl. Phys.*, 2013, **114**, 064904.

191 Y. Qian, R. Wang, B. Wang, B. Zhang and S. Gao, *RSC Adv.*, 2014, **4**, 6652–6656.

192 F. Lahoz, *Opt. Lett.*, 2008, **33**, 2982–2984.

193 F. Lahoz, C. Perez-Rodriguez, S. E. Hernandez, I. R. Martin, V. Lavin and U. R. Rodriguez-Mendoza, *Sol. Energy Mater. Sol. Cells*, 2011, **95**, 1671–1677.

194 D. Q. Chen, L. Lei, A. P. Yang, Z. X. Wang and Y. S. Wang, *Chem. Commun.*, 2012, **48**, 5898–5900.

195 X. D. Zhang, X. Jin, D. F. Wang, S. Z. Xiong, X. H. Geng and Y. Zhao, *Phys. Status Solidi C*, 2010, **7**, 1128–1131.

196 J. de Wild, A. Meijerink, J. K. Rath, W. G. J. H. M. van Sark and R. E. I. Schropp, *Sol. Energy Mater. Sol. Cells*, 2010, **94**, 1919–1922.

197 J. de Wild, J. K. Rath, A. Meijerink, W. G. J. H. M. van Sark and R. E. I. Schropp, *Sol. Energy Mater. Sol. Cells*, 2010, **94**, 2395–2398.

198 Z. Q. Li, X. D. Li, Q. Q. Liu, X. H. Chen, Z. Sun, C. Liu, X. J. Ye and S. M. Huang, *Nanotechnology*, 2012, **23**, 025402.

199 S. L. Zhao, S. Q. Xu, G. H. Jia, D. G. Deng, L. H. Huang and H. P. Wang, *Mater. Lett.*, 2011, **65**, 2407–2409.

200 Y. Chen, W. He, Y. Jiao, H. Wang, X. Hao, J. Lu and S. Yang, *J. Lumin.*, 2012, **132**, 2247–2250.

201 J. de Wild, T. F. Duindam, J. K. Rath, A. Meijerink, W. G. J. H. M. van Sark and R. E. I. Schropp, *IEEE J. Photovolt.*, 2013, **3**, 17–21.

202 S. Mathew, A. Yella, P. Gao, R. H. Baker, B. F. E. Curchod, N. A. Astani, I. Tavernelli, U. Rothlisberger, M. K. Nazeeruddin and M. Gratzel, *Nat. Photonics*, 2014, **6**, 242–247.

203 T. W. Hamann, R. A. Jensen, A. B. F. Martinson, H. Van Ryswyk and J. T. Hupp, *Energy Environ. Sci.*, 2008, **1**, 66–78.

204 K. Lee, S. W. Park, M. J. Ko, K. Kim and N. G. Park, *Nat. Mater.*, 2009, **8**, 665–671.

205 G.-B. Shan and G. P. Demopoulos, *Adv. Mater.*, 2010, **22**, 4373–4377.

206 J. Wu, J. Wang, J. Lin, Z. Lan, Q. Tang, M. Huang, Y. Huang, L. Fan, Q. Li and Z. Tang, *Adv. Energy Mater.*, 2012, **2**, 78–81.

207 J. Chang, Y. Ning, S. Wu, W. Niu and S. Zhang, *Adv. Funct. Mater.*, 2013, **23**, 5910–5915.

208 A. Khan, R. Yadav, P. K. Mukhopadhya, S. Singh, C. Dwivedi, V. Dutta and S. Chawla, *J. Nanopart. Res.*, 2011, **13**, 6837–6846.

209 C. Yuan, G. Chen, P. N. Prasad, T. Y. Ohulchanskyy, Z. Ning, H. Tian, L. Sun and H. Agren, *J. Mater. Chem.*, 2012, **22**, 16709–16713.

210 Y. Li, G. Wang, K. Pan, B. Jiang, C. Tian, W. Zhou and H. Fu, *J. Mater. Chem.*, 2012, **22**, 20381–20386.

211 L. Zhang, Q. Tian, W. Xu, X. Kuang, J. Hu, M. Zhu, J. Liu and Z. Chen, *J. Mater. Chem.*, 2012, **22**, 18156–18163.

212 G.-B. Shan, H. Assaaoudi and G. P. Demopoulos, *ACS Appl. Mater. Interfaces*, 2011, **3**, 3239–3243.

213 Y. Li, K. Pan, G. Wang, B. Jiang, C. Tian, W. Zhou, Y. Qu, S. Liu, L. Feng and H. Fu, *Dalton Trans.*, 2013, **42**, 7971–7979.

214 J. Zhang, H. Shen, W. Guo, S. Wang, C. Zhu, F. Xue, J. Hou, H. Su and Z. Yuan, *J. Power Sources*, 2013, **226**, 47–53.

215 L. Liang, Y. Liu and X.-Z. Zhao, *Chem. Commun.*, 2013, **49**, 3958–3960.

216 L. Liang, Y. Liu, C. Bu, K. Guo, W. Sun, N. Huang, T. Peng, B. Sebo, M. Pan, W. Liu, S. Guo and X.-Z. Zhao, *Adv. Mater.*, 2013, **25**, 2174–2180.

217 Z. Zhou, J. Wang, F. Nan, C. Bu, Z. Yu, W. Liu, S. Guo, H. Hu and X.-Z. Zhao, *Nanoscale*, 2014, **6**, 2052–2055.

218 P. Ramasamy and J. Kim, *Chem. Commun.*, 2014, **50**, 879–881.

219 Z. Chen, L. Zhang, Y. Sun, J. Hu and D. Wang, *Adv. Funct. Mater.*, 2009, **19**, 3815–3820.

220 X.-H. Lu, Y.-Z. Zheng, S.-Q. Bi, J.-X. Zhao, X. Tao and J.-F. Chen, *J. Power Sources*, 2013, **243**, 588–593.

221 M. J. Lim, Y. N. Ko, Y. C. Kang and K. Y. Jung, *RSC Adv.*, 2014, **4**, 10039–10042.

222 M. Liu, Y. Lu, Z. B. Xie and G. M. Chow, *Sol. Energy Mater. Sol. Cells*, 2011, **95**, 800–803.

223 X. Wu, G. Q. Lu and L. Wang, *Adv. Energy Mater.*, 2013, **3**, 704–707.

224 G. Xie, J. Lin, J. Wu, Z. Lan, Q. Li, Y. Xiao, G. Yue, H. Yue and M. Huang, *Chin. Sci. Bull.*, 2011, **56**, 96–101.

225 L. Li, Y. Yang, M. Zhou, R. Fan, L. L. Qiu, X. Wang, L. Zhang, X. Zhou and J. He, *J. Solid State Chem.*, 2013, **198**, 459–465.

226 Q. Li, J. Lin, J. Wu, Z. Lan, Y. Wang, F. Peng and M. Huang, *Electrochim. Acta*, 2011, **56**, 4980–4984.

227 H.-Q. Wang, M. Batentschuk, A. Osvet, L. Pinna and C. J. Brabec, *Adv. Mater.*, 2011, **23**, 2675–2680.

228 H.-Q. Wang, T. Stubhan, A. Osvet, I. Litzov and C. J. Brabec, *Sol. Energy Mater. Sol. Cells*, 2012, **105**, 196–201.

229 J.-L. Wu, F.-C. Chen, S.-H. Chang, K.-S. Tan and H.-Y. Tuan, *Org. Electron.*, 2012, **13**, 2104–2108.

230 A. A. D. Adikaari, I. Etchart, P.-H. Guéring, M. Bérard, S. R. P. Silva, A. K. Cheetham and R. J. Curry, *J. Appl. Phys.*, 2012, **111**, 094502.

231 W. Guo, K. Zheng, W. Xie, L. Sun, L. Shen, C. Liu, Y. He and Z. Zhang, *Sol. Energy Mater. Sol. Cells*, 2014, **124**, 126–132.

232 A. C. Pan, C. del Canizo, E. Canavos, N. M. Santos, J. P. Leitao and A. Luque, *Sol. Energy Mater. Sol. Cells*, 2010, **94**, 1923–1926.

233 W. Zou, C. Visser, J. A. Maduro, M. S. Pshenichnikov and J. C. Hummelen, *Nat. Photonics*, 2012, **6**, 560–564.

234 X. Xie, N. Gao, R. Deng, Q. Sun, Q.-H. Xu and X. Liu, *J. Am. Chem. Soc.*, 2013, **135**, 12608–12611.

235 Y.-F. Wang, G.-Y. Liu, L.-D. Sun, J.-W. Xiao, J.-C. Zhou and C.-H. Yan, *ACS Nano*, 2013, **7**, 7200–7206.